

The Extraordinary March 2022 East Antarctica “Heat” Wave. Part I: Observations and Meteorological Drivers

JONATHAN D. WILLE[Ⓜ],^{a,b} SIMON P. ALEXANDER,^{c,d} CHARLES AMORY,^a REBECCA BAIMAN,^e LÉONARD BARTHÉLEMY,^f DANA M. BERGSTROM,^{c,g,h} ALEXIS BERNE,ⁱ HANIN BINDER,^b JULIETTE BLANCHET,^a DENIZ BOZKURT,^{j,k} THOMAS J. BRACEGIRDLE,^l MATHIEU CASADO,^m TAEJIN CHOI,ⁿ KYLE R. CLEM,^o FRANCIS CODRON,^f RAJASHREE DATTA,^c STEFANO DI BATTISTA,^p VINCENT FAVIER,^a DIANA FRANCIS,^q ALEXANDER D. FRASER,^d ELISE FOURRÉ,^m RENÉ D. GARREAUD,^{k,r} CHRISTOPHE GENTHON,^s IRINA V. GORODETSKAYA,^t SERGI GONZÁLEZ-HERRERO,^{u,v} VICTORIA J. HEINRICH,^w GUILLAUME HUBERT,^x HANNA JOOS,^b SEONG-JOONG KIM,ⁿ JOHN C. KING,^l CHRISTOPH KITTEL,^a AMAELLE LANDAIS,^m MATTHEW LAZZARA,^{y,z} GREGORY H. LEONARD,^{aa} JAN L. LIESER,^{bb} MICHELLE MACLENNAN,^c DAVID MIKOLAJCZYK,^y PETER NEFF,^{cc} INÈS OLLIVIER,^{dd,m} GHISLAIN PICARD,^a BENJAMIN POHL,^{ee} F. MARTIN RALPH,^{ff} PENNY ROWE,^{gg} ELISABETH SCHLOSSER,^{hh} CHRISTINE A. SHIELDS,ⁱⁱ INGA J. SMITH,^{jj} MICHAEL SPRENGER,^b LUKE TRUSEL,^{kk} DANIELLE UDY,^{d,bb,ll} TESSA VANCE,^d ÉTIENNE VIGNON,^s CATHERINE WALKER,^{mm} NANDER WEVER,^{e,u} AND XUN ZOU^{ff}

^a Institut des Géosciences de l'Environnement, CNRS/UGA, Saint Martin d'Hères, France

^b Institute for Atmospheric and Climate Science, ETH Zurich, Zurich, Switzerland

^c Australian Antarctic Division, Kingston, Tasmania, Australia

^d Australian Antarctic Program Partnership, Institute for Marine and Antarctic Studies, University of Tasmania, Hobart, Tasmania, Australia

^e Department of Atmospheric and Oceanic Sciences, University of Colorado Boulder, Boulder, Colorado

^f Laboratoire d'Océanographie et du Climat, LOCEAN-IPSL, Sorbonne Université, CNRS, IRD, MNHN, Paris, France

^g Global Challenges Program, University of Wollongong, Wollongong, New South Wales, Australia

^h Centre for Ecological Genomics and Wildlife Conservation, Department of Zoology, University of Johannesburg, Johannesburg, South Africa

ⁱ Environmental Remote Sensing Laboratory (LTE), École Polytechnique Fédérale de Lausanne, Lausanne, Switzerland

^j Department of Meteorology, University of Valparaíso, Valparaíso, Chile

^k Center for Climate and Resilience Research, Santiago, Chile

^l British Antarctic Survey, Cambridge, United Kingdom

^m Laboratoire des Sciences du Climat et de l'Environnement, CNRS-CEA-UVSQ-IPSL, Gif sur Yvette, France

ⁿ Korea Polar Research Institute, Incheon, South Korea

^o School of Geography, Environment and Earth Sciences, Victoria University of Wellington, Wellington, New Zealand

^p Meteorio, Milan, Italy

^q Environmental and Geophysical Sciences (ENGEOS) Lab, Khalifa University, Abu Dhabi, United Arab Emirates

^r Universidad de Chile, Santiago, Chile

^s LMD/IPSL, Sorbonne Université, ENS, PSL Research University, École Polytechnique, Institut Polytechnique de Paris, CNRS, Paris, France

^t CIIMAR—Interdisciplinary Centre of Marine and Environmental Research of the University of Porto, Porto, Portugal

^u WSL Institute for Snow and Avalanche Research SLF, Davos, Switzerland

^v Antarctic Group, Agencia Estatal de Meteorología (AEMET), Barcelona, Spain

^w School of Psychological Sciences, University of Tasmania, Hobart, Tasmania, Australia

^x The French Aerospace Lab, ONERA/DPHY, University of Toulouse, Toulouse, France

^y Antarctic Meteorological Research and Data Center, Space Science and Engineering Center, University of Wisconsin—Madison, Madison, Wisconsin

^z Department of Physical Sciences, School of Engineering, Science, and Mathematics, Madison Area Technical College, Madison, Wisconsin

^{aa} National School of Surveying, University of Otago, Dunedin, New Zealand

^{bb} Institute for Marine and Antarctic Studies, University of Tasmania, Hobart, Tasmania, Australia

^{cc} University of Minnesota, Saint Paul, Minnesota

^{dd} Bjerknes Centre for Climate Research, University of Bergen, Bergen, Norway

^{ee} Biogéosciences, CNRS/Université de Bourgogne, Dijon, France

^{ff} Center for Western Weather and Water Extremes, Scripps Institution of Oceanography, San Diego, California

^{gg} NorthWest Research Associates, Seattle, Washington

^{hh} Department of Atmospheric and Cryospheric Sciences, University of Innsbruck, Innsbruck, Austria


ⁱⁱ Climate and Global Dynamics Laboratory, National Center for Atmospheric Research, Boulder, Colorado

^{jj} Department of Physics, University of Otago, Dunedin, New Zealand

^{kk} Department of Geography, The Pennsylvania State University, University Park, Pennsylvania

^{ll} ARC Centre of Excellence for Climate Extremes, University of Tasmania, Hobart, Tasmania, Australia

^{mm} Department of Applied Ocean Physics and Engineering, Woods Hole Oceanographic Institution, Woods Hole, Massachusetts

 Denotes content that is immediately available upon publication as open access.

 Supplemental information related to this paper is available at the Journals Online website: <https://doi.org/10.1175/JCLI-D-23-0175.s1>.

Corresponding author: Jonathan D. Wille, jonathan.wille@env.ethz.ch

DOI: 10.1175/JCLI-D-23-0175.1

© 2024 American Meteorological Society. This published article is licensed under the terms of the default AMS reuse license. For information regarding reuse of this content and general copyright information, consult the AMS Copyright Policy (www.ametsoc.org/PUBSReuseLicenses).

(Manuscript received 27 March 2023, in final form 25 October 2023, accepted 30 October 2023)

ABSTRACT: Between 15 and 19 March 2022, East Antarctica experienced an exceptional heat wave with widespread 30°–40°C temperature anomalies across the ice sheet. This record-shattering event saw numerous monthly temperature records being broken including a new all-time temperature record of −9.4°C on 18 March at Concordia Station despite March typically being a transition month to the Antarctic coreless winter. The driver for these temperature extremes was an intense atmospheric river advecting subtropical/midlatitude heat and moisture deep into the Antarctic interior. The scope of the temperature records spurred a large, diverse collaborative effort to study the heat wave's meteorological drivers, impacts, and historical climate context. Here we focus on describing those temperature records along with the intricate meteorological drivers that led to the most intense atmospheric river observed over East Antarctica. These efforts describe the Rossby wave activity forced from intense tropical convection over the Indian Ocean. This led to an atmospheric river and warm conveyor belt intensification near the coastline, which reinforced atmospheric blocking deep into East Antarctica. The resulting moisture flux and upper-level warm-air advection eroded the typical surface temperature inversions over the ice sheet. At the peak of the heat wave, an area of 3.3 million km² in East Antarctica exceeded previous March monthly temperature records. Despite a temperature anomaly return time of about 100 years, a closer recurrence of such an event is possible under future climate projections. In Part II we describe the various impacts this extreme event had on the East Antarctic cryosphere.

SIGNIFICANCE STATEMENT: In March 2022, a heat wave and atmospheric river caused some of the highest temperature anomalies ever observed globally and captured the attention of the Antarctic science community. Using our diverse collective expertise, we explored the causes of the event and have placed it within a historical climate context. One key takeaway is that Antarctic climate extremes are highly sensitive to perturbations in the midlatitudes and subtropics. This heat wave redefined our expectations of the Antarctic climate. Despite the rare chance of occurrence based on past climate, a future temperature extreme event of similar magnitude is possible, especially given anthropogenic climate change.

KEYWORDS: Antarctica; Atmospheric river; Extreme events; Automatic weather stations; Climate records

1. Introduction

In recent years, the repetition of many record-breaking events, significantly exceeding natural climate variability, has been described as corresponding to a pattern of human-influenced extreme events (Fischer et al. 2021). This includes the June 2021 heat wave in the Pacific Northwest (Philip et al. 2022; Thompson et al. 2022) and the July 2017 extreme flooding in Texas resulting from Hurricane Harvey (Risser and Wehner 2017). Even though the anthropogenic climate forcing is already emerging in the midlatitudes (Hawkins et al. 2020), model projections of transient anthropogenic climate change predict a slow emergence of a significant warming signal in the high southern latitudes because of the presence of the Southern Ocean (Manabe and Stouffer 1980; Hawkins and Sutton 2012), yet these models also severely underestimate the intensification of winter midlatitude storm tracks (Chemke et al. 2022).

Yet, between 15 and 19 March 2022, East Antarctica experienced a heat wave of scale and intensity never observed before with widespread 30°–40°C temperature anomalies (w.r.t. monthly mean) peaking on 18 March where record-high maximum temperatures were observed from coastal regions like Dumont d'Urville to the high Antarctic Plateau like Dome C. These austral autumnal March temperature extremes rivaled record-high maximum temperatures observed during peak summer (i.e., January). This was highly improbable, given that the Antarctic climate is usually quickly transitioning to winter conditions during March. Given the significant magnitude by which previous temperature records were exceeded, we viewed it necessary to examine the heat wave's origins,

impacts, and historical precedence to understand the consequences of events like this in the future.

As the heat wave unfolded across East Antarctica, numerical weather prediction systems and observations clearly indicated an atmospheric river (AR; Ralph et al. 2020, 2018) accompanied by a very intense atmospheric ridge throughout the depth of the troposphere, which guided subtropical/midlatitude heat and moisture deep into the Antarctic interior. This fits a pattern of other climate extremes in Antarctica being directly linked to AR landfalls (Wille et al. 2022, 2019; Francis et al. 2021; Bozkurt et al. 2018; Turner et al. 2022). ARs are narrow bands of enhanced moisture fluxes typically found ahead of an extratropical cyclone cold front embedded within the low-level jet and are responsible for most moisture transport between subtropical and polar regions (Nash et al. 2018). They have previously been linked to temperature extremes across Antarctica like the Antarctic continent maximum temperature record of 18.3°C set at Esperanza station on 6 February 2020 (Xu et al. 2021; González-Herrero et al. 2022) and the preceding record high of 17.5°C on 24 March 2015 (Bozkurt et al. 2018). In East Antarctica, ARs have been observed to induce deep, moist layers in coastal regions, contributing to record warm temperatures (Gorodetskaya et al. 2020; Turner et al. 2022). Atmospheric ridging/blocking is a prerequisite for AR landfalls in the region (Pohl et al. 2021). However, deep convection anomalies originating in the subtropics often dictate the magnitude of moisture transport and subsequent latent heat release that contribute to a baroclinic environment for extratropical cyclogenesis (Pohl et al. 2021; Terpstra et al. 2021; Clem et al. 2022; Francis et al. 2021).

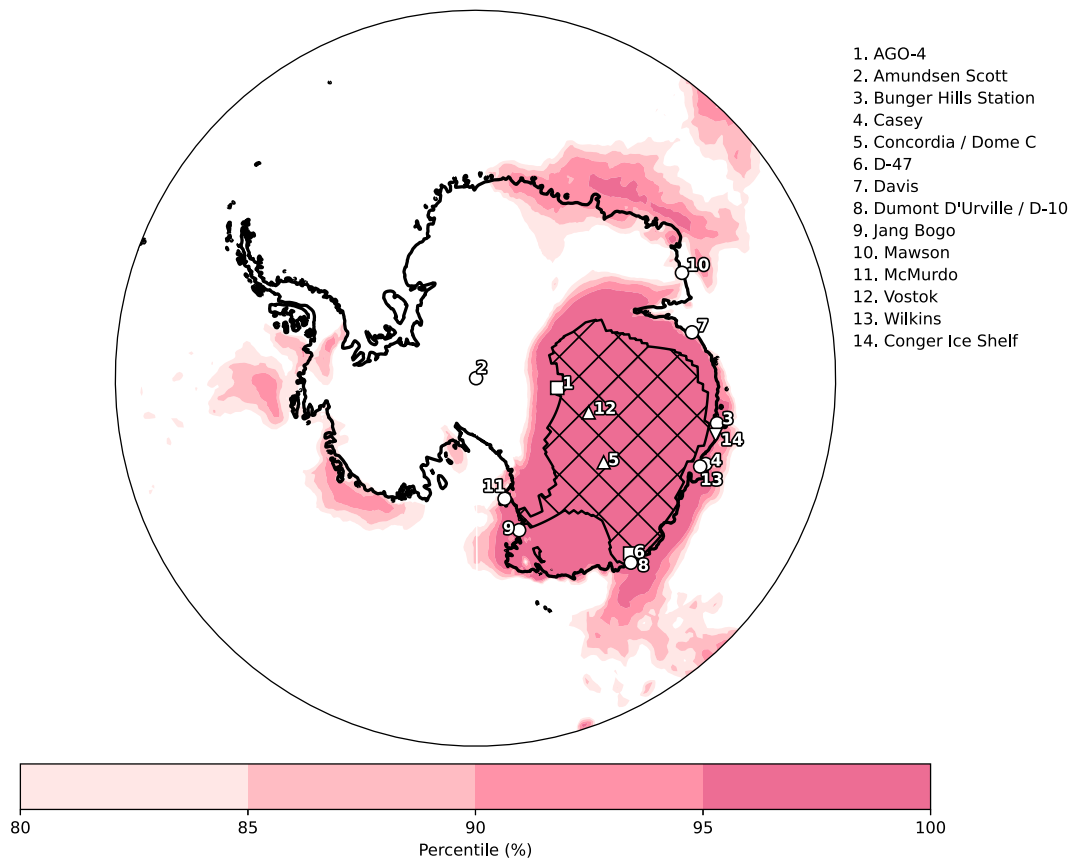


FIG. 1. Percentile of the 18 Mar 2022 mean 2-m temperature with respect to the climatological distribution of March days of the period 1979–2021 from 6-hourly daily averages. The hatched area indicates the broken temperature records on 18 Mar 2022, totaling an area of 3.3 million km². The map shows the position of the Dome C and Vostok stations (triangles) inside the hatched area, and the other research stations outside (circles), other AWS analyzed (squares) and the Conger Ice Shelf (inverted triangle) mentioned in the text. Data source: ERA5.

In this first part of our study, we present a detailed analysis of the heat wave's origins and review the multitude of broken temperature records in order to encapsulate the event's historical nature. We unravel the various atmospheric processes and impacts interacting with one another during this compound event. This is done by combining numerous different datasets and expertise to provide a detailed analysis/overview of the March 2022 East Antarctic heat wave and place this event in context with other extreme Antarctic climate events observed. We describe the subtropical origins and meteorological drivers that led to the intense AR (section 3), the scale of the temperature records (section 4), and the event's implications on the present and future Antarctic climate (section 5), concluding with a discussion on the various compounding elements of this extreme event and the challenges of calculating a return time in an environment with large temperature variability and sparse observations (section 6). For a detailed explanation of the various impacts from the March 2022 East Antarctica heat wave such as radiative forcing, surface mass balance, the collapse of the Conger Ice Shelf, sea ice extent decline, past-climate reconstruction, and

cosmic ray measurements, see Wille et al. (2024, hereinafter Part II).

2. Data and methods

a. Large-scale circulation, precipitation, melt, and moisture products

Synoptic meteorological conditions leading to the AR during the heat-wave event and the climatological context were analyzed with data from the two reanalyses ERA5 (Hersbach et al. 2020) and MERRA-2 (Gelaro et al. 2017). First, we used ERA5, produced by the European Centre for Medium-Range Weather Forecasts (ECMWF), at a global 0.25° resolution and a horizontal resolution of approximately 30 km with 137 levels. Variables including 500-hPa geopotential height (Z500), 2-m air temperature (see Fig. 1), precipitation, humidity, and horizontal wind were downloaded for 0000 UTC with daily resolution for the period 1979–2022, as well as at finer time resolution during the heat-wave event. Investigation of tropical deep convection was however performed using the NOAA interpolated outgoing longwave radiation (OLR) dataset (Liebmann and Smith 1996), at 2.5° × 2.5° horizontal

resolution. In addition, integrated vapor transport (IVT) fields were obtained from ERA5 by vertically integrating the 1-h specific humidity and zonal and meridional winds for the whole air column extending from the surface to the top of the atmosphere during the event. We also computed the meridional integrated vapor transport vIVT using MERRA-2 reanalysis data, which is at a resolution of 0.5° latitude by 0.625° longitude. Both reanalyses could be used here to initialize the polar specific AR detection algorithm from Wille et al. (2021), but only results of the detection algorithm using MERRA-2 are presented here. A full description of the detection algorithm can be found in Wille et al. (2021). This algorithm uses a relative vIVT threshold designed to specifically capture poleward moisture fluxes (Shields et al. 2022; Collow et al. 2022).

b. Clouds and impacts on the energy balance

We analyzed AR impacts on the surface snow energy budget using the Polar Weather Research and Forecasting (PWRF) Model, version V4.3.3, to provide high-resolution simulations, especially for radiative terms. Among multiple model simulations assessed using broadband downwelling radiance data observed at Dome C (Figs. S5 and S6 in the online supplemental material), we found that the best performance was exhibited by PWRF driven by ERA5 reanalysis data, particularly during the event's peak. Previous research has consistently confirmed PWRF's reliability in providing reasonable cloud information and surface energy balance estimates for polar regions (Zou et al. 2021, 2023; Djoumna and Holland 2021; Andernach et al. 2022; Gorodetskaya et al. 2023). To better describe the cloud liquid water and its impacts on the surface energy balance, the more advanced microphysics scheme was selected, namely the two-moment Morrison–Milbrandt P3 (P3) scheme (Hines et al. 2019; Listowski et al. 2019). For the atmospheric boundary layer, this study used the Mellor–Yamada–Nakanishi–Niino turbulence scheme (MYNN; Nakanishi and Niino 2006). The Rapid Radiative Transfer Model for GCMs (RRTMG) was used for both longwave and shortwave radiation. In addition, the Kain–Fritsch scheme was selected for cumulus parameterization, and Noah–MP was chosen for the land surface model (Kain 2004; Niu et al. 2011). High-resolution topography information from the Reference Elevation Model of Antarctica (REMA) and MODIS surface observed albedo were included in the input data to better simulate the surface conditions (Howat et al. 2019; Corbea-Pérez et al. 2021). See the methods section in Part II for details on the SNOWPACK surface energy balance calculations.

c. Return period analysis of the extreme event

Temperature data from Amundsen Scott (2835 m), Casey (42 m), Davis (13 m), Dome C (3233 m), Dumont d'Urville (43 m), Mawson (16 m), McMurdo (24 m), and Vostok (3488 m) are considered to estimate the return periods of the mid-March 2022 event across the East Antarctic Ice Sheet (Fig. 1; appendix B describes in more detail the measurement sites used in this study). Instantaneous temperature records, at 3-h

frequencies, were examined from these from at least 1980 (minimum 1956) and to the end of March 2022. Daily minima (TN), daily maxima (TX), and daily means (Tmean) were considered together with their anomalies by subtracting the daily averages over the whole period from the daily values. Return periods estimation follows extreme value theory (Coles 2002), which states that peaks over a large threshold can be modeled by the generalized Pareto distribution (GPD) whose cumulative distribution function is given by

$$F_{(\mu, \sigma, \xi)}(T) = 1 - [1 + \xi(T - \mu)/\sigma]^{(-1/\xi)} \quad (1)$$

for any (raw or anomaly) temperature T exceeding the large threshold μ . The GPD scale ($\sigma > 0$) and shape ($\xi \in \mathbb{R}$) parameters model respectively the variability and the tail-heaviness of the peaks. In this study, the threshold μ was set to the 98th percentile, so on average about 7 exceedances per year are considered at each station. However, we also checked that the 97th and 99th percentiles (3–11 exceedances per year) gave similar results. The GPD parameters (σ , ξ) were estimated at each station with the maximum likelihood method. The return period of a given extreme temperature T (exceeding μ) is then given by (Coles 2002)

$$RP(T) = 1/\{n \times p \times [1 - F_{(\mu, \sigma, \xi)}(T)]\}, \quad (2)$$

where $n = 365.25$ and $p = 1 - 0.98$. Confidence intervals were obtained by parametric bootstrap (Efron and Tibshirani 1994) drawing 500 GPD samples at each station.

d. Heat-wave magnitude in relation to historical and future climate variability

To better characterize the statistics of the March 2022 extreme heat-wave event and as a first approach to examine the likelihood of future occurrence of similar events, it is necessary to use a general circulation model. We used the ensemble simulations performed for phase 6 of the Coupled Model Intercomparison Project (CMIP6) by the Institut Pierre Simon Laplace (IPSL) model (IPSL-CM6; Boucher et al. 2020). We extracted the daily 2-m temperature values close to Dome C (123°E , 73°S) over two time periods: 1) a historical period (1980–2015), with 20 ensemble members, and 2) a future period (2035–70) for two different shared socioeconomic pathway (SSP) scenarios, SSP2-4.5 and SSP3-7.0, with 10 ensembles members each. The physics of the IPSL-CM6 model contains specific improvements to reliably represent the boundary layer structure and near-surface temperatures over the Antarctic. The spatial resolution is 2.5° in longitude and 1.267° in latitude. To confirm the reliability of the model temperature distribution, the probability distribution functions (PDFs) of the temperature anomalies with respect to monthly means for the model and for the AWS temperature measurements at Dome C are compared (Fig. S1 in the online supplemental material). The two PDFs are very similar to each other, giving confidence in using the temperature anomalies determined from the model for use in this study.

Table S1 in the online supplemental material summarizes the type and purpose of the reanalysis, model, and instrumental data utilized in this study.

3. Meteorological drivers

a. Local and nonlocal background circulation

The East Antarctic heat-wave conditions (15–19 March 2022) that peaked on 18 March 2022 were the product of the synchronization of various compound synoptic weather patterns of subtropical origins that occurred over the two weeks prior to the eventual AR landfall (Fig. 2). The moisture that reached Antarctica (and leading up to the extreme event) primarily originated over the central and southwest subtropical Indian Ocean and was related to tropical storm and cyclone activity.

The 2021/22 tropical cyclone (TC) season in the Indian Ocean sector was particularly late to start (TC Ana; 24 January). However, March was very active, and the cyclonic season ultimately was above normal in terms of cyclogenesis and TC development. Between late February and late March (25 February–25 March 2022), 12 tropical storms developed in the Indian Ocean sector, with five becoming TCs based on the Saffir–Simpson scale. Several TCs occurred within a few days of one another. Possible explanations involve the La Niña conditions over the 2021/22 season, and a particularly strong (93rd percentile) Madden–Julian oscillation (MJO; Zhang 2005) that persisted over the Indian Ocean sector between 13 and 21 March. These combined conditions have been shown to promote favorable environments for TC development, and more generally for convective activity over the Indian Ocean sector (Ho et al. 2006; Kuleshov et al. 2008) and nearby southern Africa (Cook 2001; Pohl et al. 2007). La Niña conditions and an active Indian Ocean MJO also increase the intensity (La Niña also increases frequency) of tropical–temperate troughs (TTTs) over the African landmass that contribute 30%–60% of summer rainfall over southern Africa (Fauchereau et al. 2009; Pohl et al. 2018; Hart et al. 2013; Macron et al. 2014). TTTs form when midlatitude Rossby waves interact with tropical African convection, resulting in elongated bands of intense convection, rainfall, and poleward moisture export over the southwest Indian Ocean (Fauchereau et al. 2009).

The development of multiple tropical storms and a TTT in short succession was key to preconditioning the environment responsible for the East Antarctic heat-wave event. The first Indian Ocean tropical cyclone related to the East Antarctic heat-wave event was TC Vernon, which formed on 25 February southwest of Christmas Island and reached category 4 on the Saffir–Simpson scale. TC Vernon dissipated slowly while moving southward between 2 and 4 March. Between 6 and 10 March it stalled over the central Indian Ocean near 35°S, 90°E, due north of Davis Sea, East Antarctica, and gradually transitioned into an extratropical cyclone. During this time, ex-TC Vernon advected a record-high plume (Fig. 2c) of deep tropical moisture to the central Indian Ocean between 30° and 45°S, which would eventually be transported to East Antarctica in the days leading up to the heat-wave event.

Meanwhile, to the west of Vernon, TC Gombe developed near Madagascar on 9 March, and underwent rapid intensification as it slowly tracked westward toward Mozambique during 10–12 March. Upstream to the west of TC Gombe, a very strong (96th percentile) TTT (Macron et al. 2014; Hart et al. 2010) developed in the South Atlantic on 9 March and tracked eastward toward southern Africa (and TC Gombe) between 9 and 12 March, where it then merged with the remnants of TC Gombe on 13–14 March. This formed a second distinct reservoir of deep tropical moisture that extended from southern Africa poleward to ~60°S over the Southern Ocean, which would later merge with TC Vernon's moisture plume to the east and arrive in East Antarctica on 17–18 March.

Furthermore, the evolution of the synoptic circulation pattern during 15–18 March that eventually allowed the moisture to advect deep into East Antarctica was influenced by a third tropical cyclone, TC Billy. TC Billy formed on 15 March in the eastern Indian Ocean northwest of Australia and tracked southwest into the central Indian Ocean. On 15–16 March, a Rossby wave source became established to its south and anomalous poleward stationary wave fluxes developed on the southern edge of TC Billy's deep convection. This developed and shifted the preceding circulation anomalies emanating from Madagascar eastward into the central Indian Ocean and slightly poleward, now emanating from near TC Billy near 30°S, 90°E. Importantly, the eastward and poleward development of the circulation pattern helped further build the blocking ridge along the East Antarctic coast, and the ridge began to develop poleward into the interior of East Antarctica. As the circulation anomalies amplified and shifted east and poleward on the 16th, the moisture plume from Gombe/TTT, already in transit across the Southern Ocean to East Antarctica, was rapidly transported poleward to the East Antarctic coast. On 17–18 March, the large-scale circulation over the Indian Ocean became disconnected from the tropical convection, and the East Antarctic ridge became cut off from the main midlatitude wave packet. In this final act, the cutoff ridge shifted south into East Antarctica and on its western edge it advected the remaining and accumulated tropical moisture along the East Antarctic coast deep into the interior during 17–18 March, culminating in the extraordinary heat wave on 18 March.

Altogether, two distinct reservoirs of deep tropical moisture associated with three separate tropical cyclones were both transported to the same region of East Antarctica during 14–18 March. The moisture transport pathway, stretching from southern Africa eastward into the central Indian Ocean and then poleward to East Antarctica, remained quasi-stationary over this period allowing for rapid and uninterrupted transport of both moisture plumes. The quasi-stationary and great circle structure of the circulation anomalies were both formed and maintained by two regions of anomalous deep tropical convection, the first occurring near Madagascar during 13–15 March associated with the strong and persistent MJO event, and the second being TC Billy during 15–16 March, which slightly shifted the pattern eastward and poleward. In the midlatitudes, the strong ridge along the East Antarctic coast (associated with an anticyclone southeast of Australia) that remained

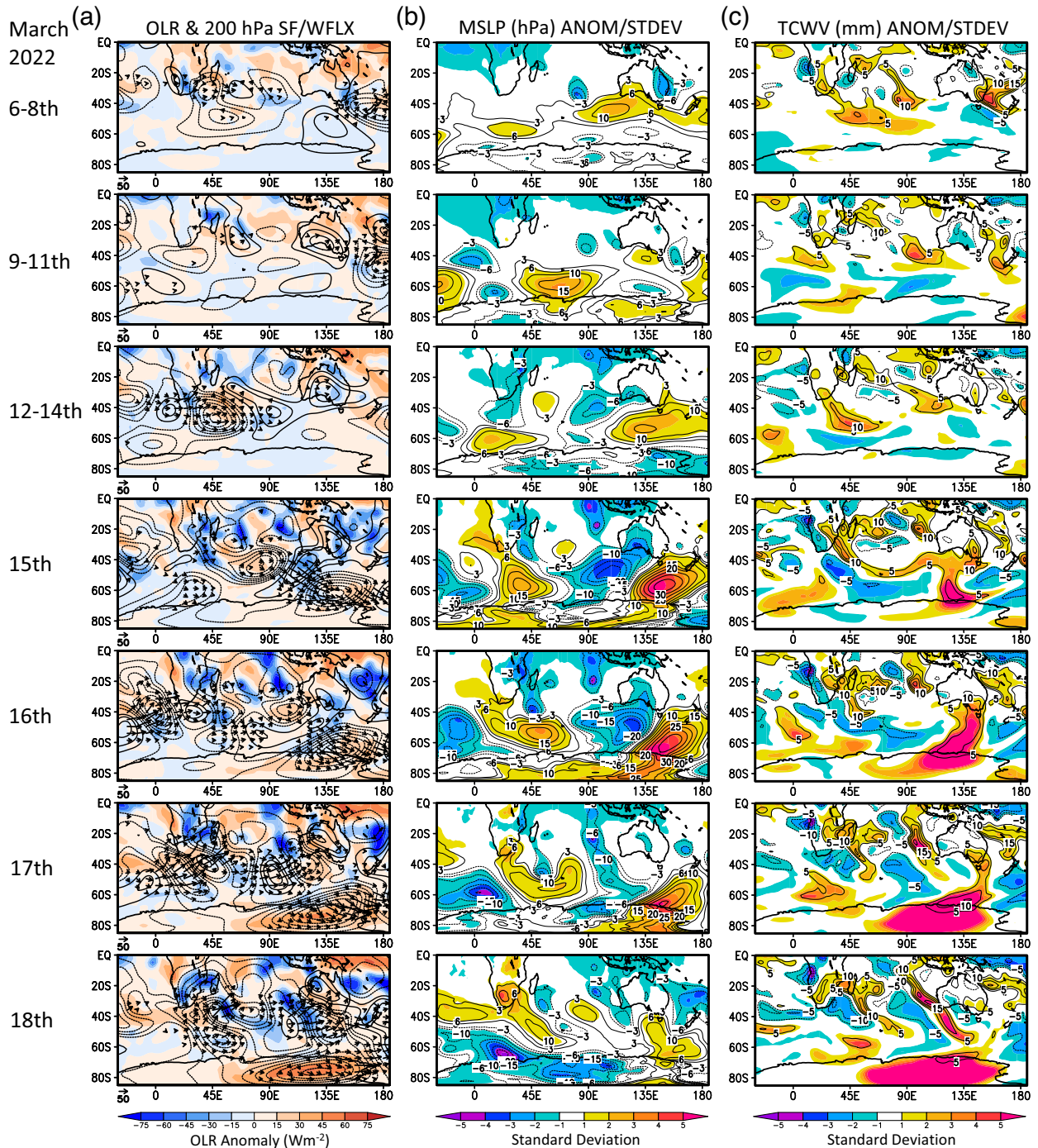


FIG. 2. The March 2022 (a) daily outgoing longwave radiation (shaded; W m^{-2}), 200-hPa streamfunction (contours: dashed = negative, and solid = positive), and 200-hPa stationary wave flux anomalies (vectors; $\text{m}^2 \text{s}^{-2}$; Takaya and Nakamura 2001), (b) daily mean sea level pressure anomalies (contours; hPa) and standard deviations (shaded), and (c) daily total column water vapor anomalies (contours; mm) and standard deviations (shaded). Anomalies and standard deviations are based on the centered 5-day-running-mean long-term mean over 1979–2021. Units for shaded anomalies are shown in the color bar at the bottom of each column. Source: NOAA Interpolated OLR and ERA5.

quasi-stationary while intensifying throughout this period was crucial for maintaining the moisture transport into high latitudes and was itself embedded in a prominent zonal wave-3 pattern (e.g., Bergstrom et al. 2018; Goyal et al. 2021) that was

particularly strong between 55° and 60°S (not shown). Finally, the ridge that became cut off from the midlatitude storm track on 17–18 March and moved poleward into East Antarctica pushed the moisture deep onto the plateau.

Over Antarctica, the end result of these various meteorological drivers is visualized in Fig. 3, which shows averaged anomalies of Z500, near-surface air temperature, and wind vectors for the 14–20 March 2022 period with respect to 1979–2021 March climatology. A clear midlevel ridge pattern extends from New Zealand and southeast Australia toward east Antarctica. Along the coastal zone and over the inland plateau of east Antarctica, Z500 was more than around 200 m ($>+2$ std dev) and this anomalous midlevel circulation anomaly results in anticyclonic circulation at the surface. At the same time, each flank of the midlevel ridge exhibits midtropospheric low and cyclonic circulation at the surface. These strong circulation anomalies triggered northerly warm-air and moisture advection toward east Antarctica on the eastern flank of the midlevel ridge, resulting in extreme warm anomalies of around 20°C across the east Antarctic plateau. In the next section, moisture transport under the abovementioned synoptic conditions is explored.

b. Inland moisture advection

The aforementioned synoptic weather patterns created ideal conditions for an AR family event to occur along the East Antarctic coastline (MacLennan et al. 2023). Unlike most AR events, the landfall on 18 March extended well beyond the coastline and transported moisture deep into the Antarctic interior. According to a polar specific AR detection algorithm, the AR landfall began on 14 March west of Dumont d'Urville station reaching an initial intensity peak on 0600 UTC 15 March when using IVT as a measure of intensity (Fig. 4). When comparing the IVT of this AR event with the IVT of all AR landfalls along the East Antarctica coastline (160°E – 20°W) from 1980 to March 2022, the first intensity maximum on 0300 UTC 15 March was in the 89.5th percentile and most of the moisture transport remained confined to the coastline. Following a brief lull after the initial wave of moisture advection, the IVT increased again later on 15 March, indicating the arrival of a second moisture flux. In addition, a deep ridge built over the East Antarctica interior pushed the AR moisture flux farther inland. By 17 March, the moisture advection advanced far inland with an AR being detected over Dome C. This is also when the AR intensity reached an absolute maximum at the coastline. The IVT reached 958 kg m s^{-1} , which is the absolute record maximum IVT value for the entire East Antarctic coastline and is 8.17 standard deviations from the mean AR IVT [as compared with all AR detections from 1980 to 2022 according to the AR detection algorithm in Wille et al. (2021)]. Intense AR conditions continued throughout 18 March until the last AR detection at 1500 UTC. Overall, this AR event was one of the longest AR events detected along the East Antarctic coastline and was by far the most intense when comparing the cumulative IVT with 2226 other detected AR events since 1980 (Fig. 5). Using the AR intensity scale described in Ralph et al. (2019), this event would be classified as an AR category 4 (just $\sim 50\text{ kg m s}^{-1}$ shy of being an AR category 5), and would be considered an extreme, hazardous storm by midlatitude standards.

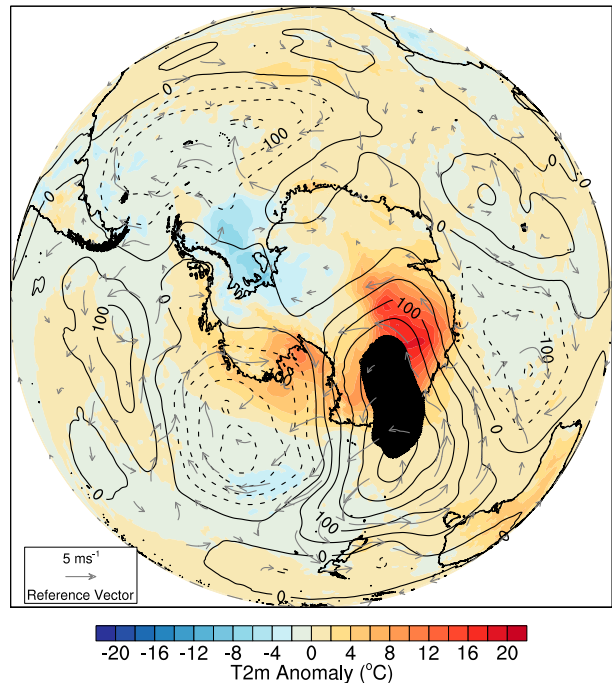


FIG. 3. Averaged anomalies of Z500 (m; contours), near-surface air temperature ($^{\circ}\text{C}$; shaded), and 10-m wind vectors (m s^{-1}) for the 14–20 Mar 2022 period with respect to the 1979–2021 March climatology. Hatching indicates the grid points where Z500 anomalies are larger than 2 std dev. Data source: ERA5.

Infrared satellite composite imagery showed a prolonged advection of clouds associated with the AR that initially remains near the coastline during the first wave of AR moisture around 15 March before penetrating deep into the Antarctic interior over the next few days (see the animation in the online supplemental material). Although poleward moisture advection ended after 18 March, there was a very evident counterclockwise flow of clouds around a blocking anticyclone that trapped residual AR moisture in the Antarctic interior (Fig. S2 in the online supplemental material). This kept surface temperatures elevated for many days after the AR event.

The AR evolution can also be examined through the lens of mass continuity in Fig. 4b. Spatial and temporal maxima in IVT correspond with maxima in upper-level divergence and lower-level moisture convergence, showing lifting of moist air associated with the AR. From 16 to 17 March the upper-level trough (shown in black contours in Fig. 4a) develops a negative horizontal tilt favorable to cyclone development associated with a strengthening of upper-level divergence and lower-level convergence, enhancing AR-associated cloud formation and precipitation. By 18 March, there was a break in the corridor of the low-level moisture convergence between the midlatitudes and polar regions.

To understand the link between the AR in the lower troposphere and the formation of the pronounced upper-level ridge, the occurrence of warm conveyor belts (WCBs) was investigated. WCBs are strongly ascending warm and moist

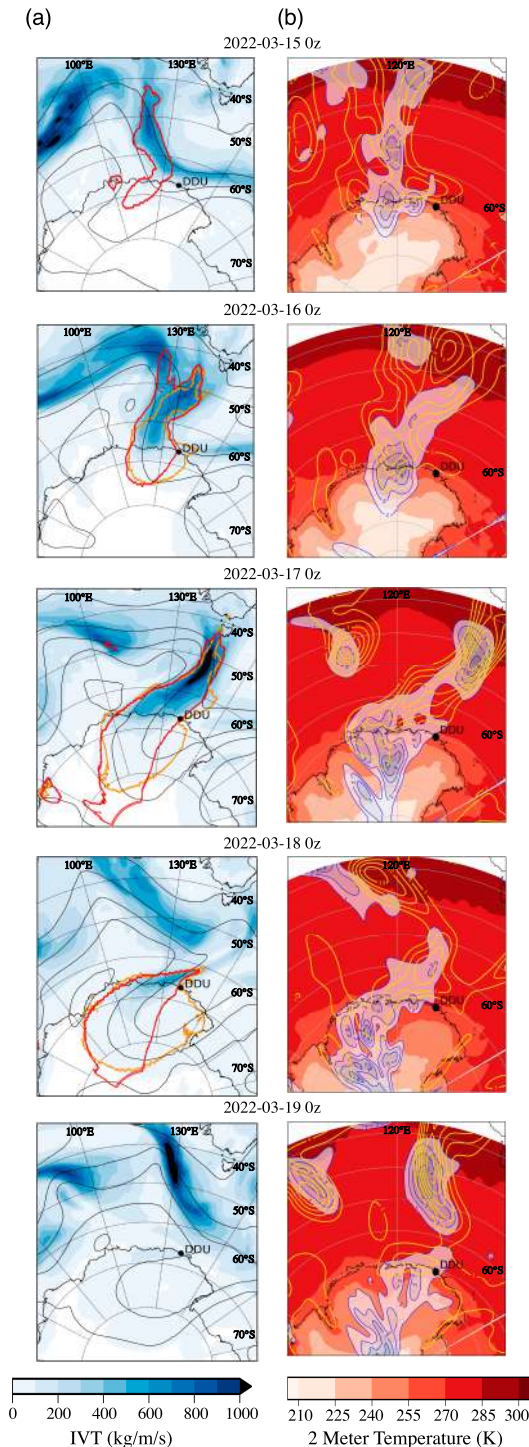


FIG. 4. Daily time steps from MERRA-2 reanalysis: (a) integrated vapor transport (IVT; $\text{kg m}^{-1} \text{s}^{-1}$) in blue-shaded contours, AR objects detected using IWV in red outlines, and AR objects detected using IWV in orange outlines and (b) 2-m temperature ($^{\circ}\text{C}$) in red-shaded contours, 250-hPa divergence (10^{-5} s^{-1}) in blue contours, and 10-m moisture convergence ($10^{-5} \text{ g kg}^{-1} \text{ s}^{-1}$) in yellow contours. Dumont d'Urville (DDU) is shown on the coast of Adélie Land, East Antarctica.

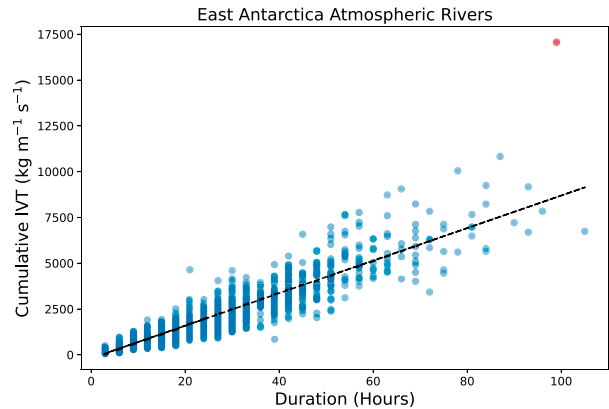


FIG. 5. Every AR landfall across East Antarctica from January 1980 to March 2022 and their respective duration and cumulative IVT. The March 2022 AR event is highlighted in red. Cumulative IVT is the summation of the maximum IVT values observed within the AR for each 3-h time step in which an AR is detected. The range considered for AR landfalls extends from 160°E to 20°W and includes 2226 distinct AR events. The black dashed line is the linear trend.

airstreams in extratropical cyclones (Green et al. 1966; Harrold 1973; Carlson 1980). They originate in the warm sector of the cyclone and ascend in approximately two days to the upper troposphere. Because of the strong ascent, they are associated with the formation of an elongated cloud band and most of the precipitation in extratropical cyclones (Browning 1986; Wernli 1997). The latent heat release occurring during cloud formation leads to a strong diabatic modification of potential vorticity (PV; Wernli and Davies 1997). WCBs therefore reach the upper troposphere with (absolute) low [~ 0.5 potential vorticity units (PVU; $1 \text{ PVU} = 10^{-6} \text{ K kg}^{-1} \text{ m}^2 \text{ s}^{-1}$)] PV values and therefore can contribute to or amplify the formation of upper-tropospheric ridges. For this analysis, WCB trajectories were calculated based on the ERA5 reanalysis data, with starting points on an equidistant (80 km) horizontal grid and on 14 levels from surface up to 200 hPa.

Originating from the AR that reached Dumont d'Urville Station, a long-lived, pronounced WCB evolved. It started its ascent in the extremely moist environment of the AR and ascended to the upper troposphere. WCB trajectories ascended continuously in this area starting already on 1200 UTC 13 March. As an example, Fig. 6a shows WCB trajectories that initiated their ascent on 1800 UTC 16 March and were associated with an extratropical cyclone around 120°E . In the following two days, the WCB ascended to approximately 400–300 hPa, thus reaching the upper troposphere, whereas the main ascent occurred along the Antarctic coastline. Because of the strong diabatic PV modification, the WCB reached the upper-tropospheric levels with PV values around -0.5 PVU, which represents a strong positive PV anomaly at those pressure levels over Antarctica. In Fig. 6b, PV on the 310-K isentrope is shown on 0000 UTC 18 March, representing the upper-level wave pattern. A pronounced upper-level ridge was present over large parts of East Antarctica, downstream of the surface cyclone. The intersection

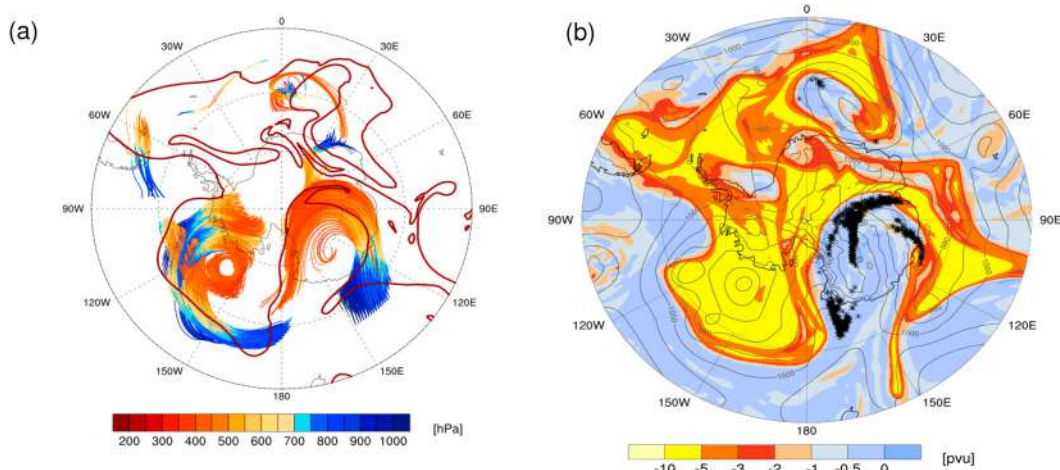


FIG. 6. (a) The 48-h forward WCB trajectories starting on 1800 UTC 16 Mar in the lower troposphere and ascending from the AR within 2 days to the upper troposphere and ending in the pronounced upper-level ridge over East Antarctica. The trajectories are colored with pressure; the thick red line shows the -2 PVU isoline on 310 K. (b) Intersection of the WCB trajectories with the 310-K isentrope at 1800 UTC 16 Mar (black crosses). In addition, PV (PVU) is shown in color on the 310-K isentrope, highlighting the pronounced upper-level ridge over East Antarctica into which the WCB air masses of high PV feed. The thin gray lines show sea level pressure on 16 Mar with a contour interval of 10 hPa.

points of the WCB air with the 310-K isentrope are marked by black crosses. In summary, the WCB air masses reached this altitude (310-K isentrope) with very high PV values around -0.5 PVU, became located inside the high-PV area of the ridge and helped to amplify the upper-level ridge. A Hovmöller diagram of 300 hPa PV anomalies confirms that the ascent of WCB parcels aligned with intense moisture advection led to positive PV anomalies starting on 13 March and reached a maximum in magnitude and extent on 18 March when the upper-level ridge was at its greatest extent (Fig. S3 in the online supplemental material). The WCB, therefore, can be considered as the link between the low-level high moisture area of the AR where it originated from and the pronounced upper-level ridge, which further determined the upper-level flow.

c. Clouds, radiation, and surface energy balance

Observations of other AR and moisture intrusion events over the Antarctic interior have indicated that the presence of cloud liquid water and resulting radiative forcing are the main drivers of temperature increases (Djoumna and Holland 2021; Wille et al. 2019; Schlosser et al. 2016). This also appeared to be the case over Dome C during the March 2022 heat-wave event. As shown in Fig. S5 in the online supplemental material, before the event, the low sun elevation angles and high surface albedo meant that the daily average downward and net shortwave radiations (orange bars in top and middle panels) were low enough that the net shortwave radiation was approximately balanced by the (negative) net longwave radiation, resulting in a total net radiation near zero (bottom panel).

During 12–15 March, this situation roughly persisted, with a slight reduction in net downward shortwave, while the small increases in the downward longwave were more than offset by increases in the upwelling longwave due to increasing

surface temperature, so that the net longwave radiation remained constant at around -30 W m^{-2} (Fig. 7b). However, starting on 15 March, the increased cloudiness and humidity caused the downwelling longwave radiation to increase markedly, from $\sim 100 \text{ W m}^{-2}$ (daily mean) to almost triple that by 19 March. Over the same period, the liquid water path increased to 50 g m^{-2} on 19 March 2022 (see Fig. S4 in the online supplemental material; prior to this time the data are missing because of snow on the sensor). The increase in the downwelling longwave more than outpaced the concomitant decrease in the shortwave (reduction in net daily average shortwave from 20 to 7 W m^{-2}), leading to positive values for the net broadband radiation over 15–20 March (daily averages ranging from 5 to 23 W m^{-2}). Indeed, the net daily average longwave radiation was itself positive over 16–18 March and was roughly equivalent to the net daily shortwave radiation. Positive net longwave radiation requires that the temperature aloft (e.g., cloud temperature) be greater than the surface temperature, which was possible because of the extreme temperature inversion; on 16 March the temperature inversion was still $\sim 20^\circ\text{C}$, and even at the peak warming on 18 March it was $\sim 10^\circ\text{C}$ (see Fig. 10, described in more detail below).

Thus, at Dome C, the clouds brought in by the AR allowed sunlight through, while at the same time the clouds, humidity, and surface inversion were strong enough to flip the typical March pattern for net longwave from one of strong cooling to a warming on a par with that from the net solar radiation. The same trends are seen in ERA5 and PWRP data near Dome C (Figs. S5 and S6 in the online supplemental material), although details differ, likely due to variability in cloud properties. For the East Antarctic Ice Sheet as a whole, PWRP results indicate that trends are similar to those seen at Dome

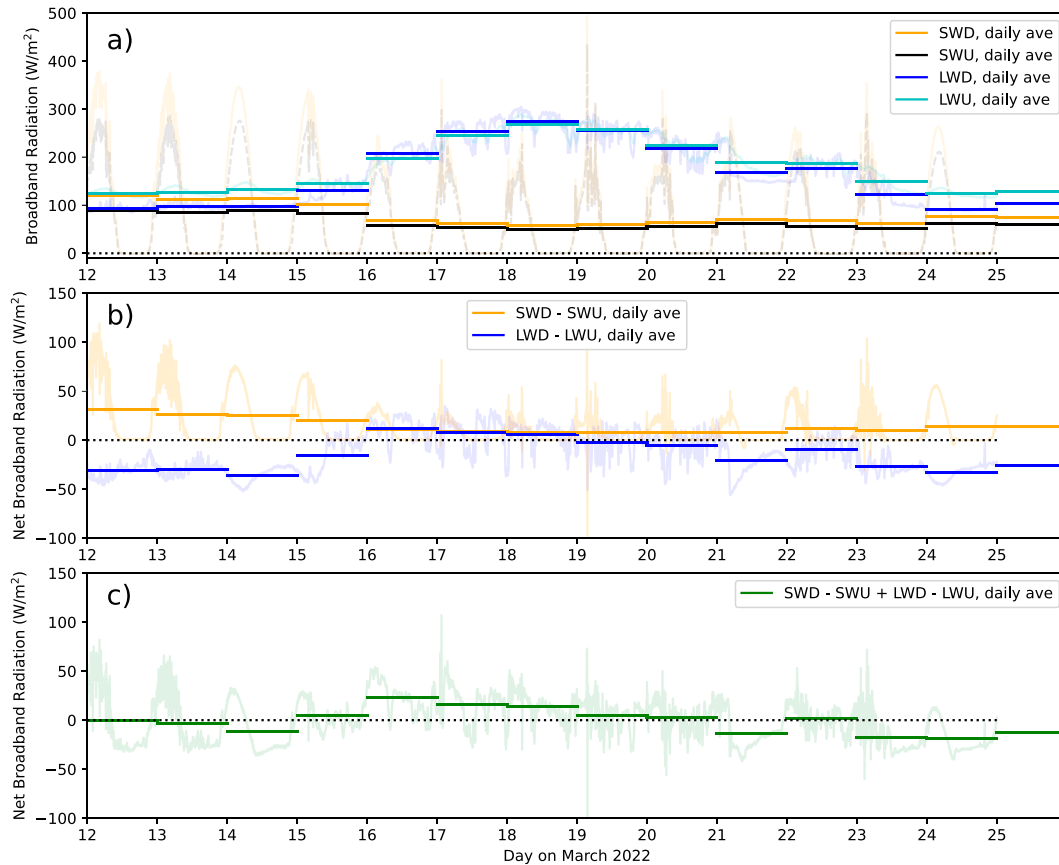


FIG. 7. Broadband radiation measurements made from the surface at Dome C, Antarctica, during 12–25 Mar 2022: (a) shortwave downward (SWD) and upward (SWU) radiation and longwave downward (LWD) and upward (LWU) radiation, (b) net broadband radiation (down – up) for shortwave and longwave, and (c) net broadband radiation. The faint lines in (a)–(c) represent the instantaneous measurements, and horizontal bars indicate daily averages.

C, with significant shortwave radiation penetrating the clouds during daytime (Figs. 8a,c) and downwelling longwave radiation strong enough to lead to positive net longwave radiation over much of East Antarctica (Figs. 8b,d), contributing to high 2-m temperatures (Fig. 8e).

The surface energy balance (SEB; the algebraic sum of the radiative and turbulent heat fluxes at the surface) as calculated by SNOWPACK is also consistent with the observations at Dome C and reveals a strong positive SEB for a large area on the East Antarctic Ice Sheet (see the methods section in Part II for a description of SNOWPACK). In March, the transition from summer to winter is typically associated with a negative SEB but, averaging over the 5-day heat wave, the anomaly in the SEB was large and positive (5–20 W m^{-2} ; Fig. S7a in the online supplemental material) and significantly larger than the climatological mean (Fig. S7b). We find that this is 4–6 times the climatological standard deviation for this period above the mean (Fig. S7c). In general, the largest positive deviations in the SEB are primarily driven by cloud-induced downwelling longwave radiation that is only slightly offset by relatively small decreases in shortwave radiation. See Fig. A1 in appendix A for a further explanation of the SEB individual components.

Climatologically, sublimation from the surface is the dominant process over large areas of the Antarctic ice sheet (Agosta et al. 2019). However, with the earlier discussed small difference in surface and air temperature, sublimation was strongly reduced, possibly even to the extent that deposition occurred (see Figs. S2d–f in the online supplemental material in Part II). Thus, even though the anomaly in latent heat flux was small with respect to the other SEB components from a climatological point of view (Fig. A1k), it was 20–30 times the standard deviation above normal (Fig. A1l). (Further discussion of contributions to the SEB is given in appendix A).

4. Temperature observations and records

a. Temperature observations

The unusually strong AR caused exceptionally strong temperature anomalies over East Antarctica that peaked around 18 March. Vostok Station, on the high plateau of East Antarctica, initiated weather observations in January 1958. The temperature of -17.7°C observed at 0814 UTC 18 March 2022 was the highest in the record for March, which exceeds the previous March record of -32.6°C (at 0600 UTC 4 March

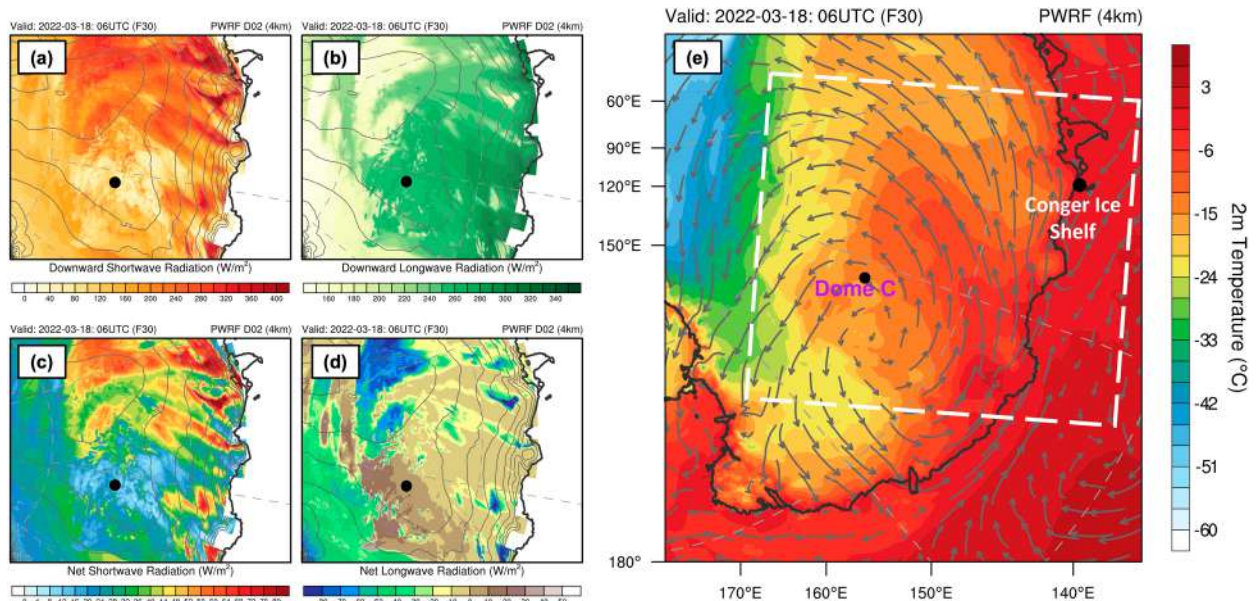


FIG. 8. PWRP model results for (a) downwelling shortwave radiation, (b) downwelling longwave radiation, (c) net shortwave radiation, and (d) net longwave radiation, along with (e) 2-m temperature. All radiation values are in watts per meter squared. The large dot indicates the location of Dome C, and the white dashed polygon in (e) shows the zoom-in domain for the radiation in (a)–(d). Contour lines correspond to topography, and vectors correspond to 10-m wind.

1967) by nearly 15°C . In the entire record of Vostok before March 2022, only in the austral summer months (December and January) did temperatures exceed -20°C . The highest 2-m air temperature recorded at the station was -12.2°C on 11 January 2002. In the period of nonsummer months (February–November) the preceding maximum values were -22.2°C on 6 February 2009 and -22.0°C on 23 November 1974.

At Concordia Station, Dome C, the previous absolute maximum was -13.7°C recorded on 0136 UTC 17 December 2016. Before the installation of the Concordia staffed station, in 1980 the Antarctic Meteorological Research Center (AMRC) installed the nearby Dome C AWS (74.50°S, 123.00°E; 3280 m). Since 1996 the site has been renamed Dome C II (75.11°S, 123.35°E; 3250 m). On 0440 UTC 18 March 2022 the sensor recorded -9.4°C (with a wind speed 7.5 m s^{-1}) setting a new absolute maximum temperature record, beating the previous record of -10.0°C on 2 January 2002, and shattering the previous March record of -27.6°C on 0610 UTC 17 March 1996.

Figure 9 shows University of Wisconsin–Madison AWS temperature and pressure observations at Dome C II (Fig. 9a), D-47 (Fig. 9b), D-10 (Fig. 9c), and AGO-4 (Fig. 9d) over March 2022 (see their location in Fig. 1). Before the AR arrived, temperatures were oscillating around -55°C (i.e., near-climatological mean temperature of -53.4°C for this time of the year), then pressure began to increase, followed by temperatures (Fig. 9). Temperatures decreased in the days following the record back to mean values around 23 March. Dome C II AWS observed the strongest magnitude warming as the temperature anomaly reached 44.0°C ($+6.0$ sigma) above its mean March climatological temperature (Fig. 9a). While warming signatures of similar magnitude were observed at the other three AWS,

the departures from the mean climatological temperatures were greatest at the inland sites (Dome C II AWS and AGO-4 AWS). The AGO-4 AWS temperature reached a maximum of -27.6°C ($+29.4^{\circ}\text{C}$, $+4.7$ sigma) with a wind speed of 11.3 m s^{-1} at 1820 UTC 18 March, D-47 AWS reached a maximum of -3.3°C ($+20.7^{\circ}\text{C}$, $+4.1$ sigma) with a wind speed of 13.6 m s^{-1} at 0610 UTC 18 March, and D-10 AWS reached a maximum of 2.9°C ($+15.1^{\circ}\text{C}$, $+3.7$ sigma) with a wind speed of 8.5 m s^{-1} at 0110 UTC 18 March. As the temperature increased during the warming event, the pressure increased as well, but with a few days lead on the temperature. After 18 March, as the warming event ended, temperature at the four sites followed a cooling trend for the remainder of the month. By 31 March, each AWS had temperatures at or just below the monthly mean temperature.

Figure 10 shows temperature profiles in the lowest 2000 m above Concordia station from radiosondes launched at around 1200 UTC each day from 12 to 22 March. On 12 March the profile was typical of that seen at the station during the extended winter months. A strong ($\sim 21^{\circ}\text{C}$) temperature inversion extended from the surface to around 380 m above ground level. From 13 to 18 March the air just above the surface inversion warmed by around 30°C as the AR moved over the station. Over the same period the surface temperature increased considerably more, by $\sim 40^{\circ}\text{C}$, reducing the strength of the surface inversion to around 7°C . Throughout this period, near-surface wind speeds at the station remained moderate ($\sim 5\text{ m s}^{-1}$), suggesting that the erosion of the surface inversion was largely caused by changes in surface energy balance driven by the intrusion of the warm/moist air mass aloft, rather than by increased shear-driven turbulent mixing within

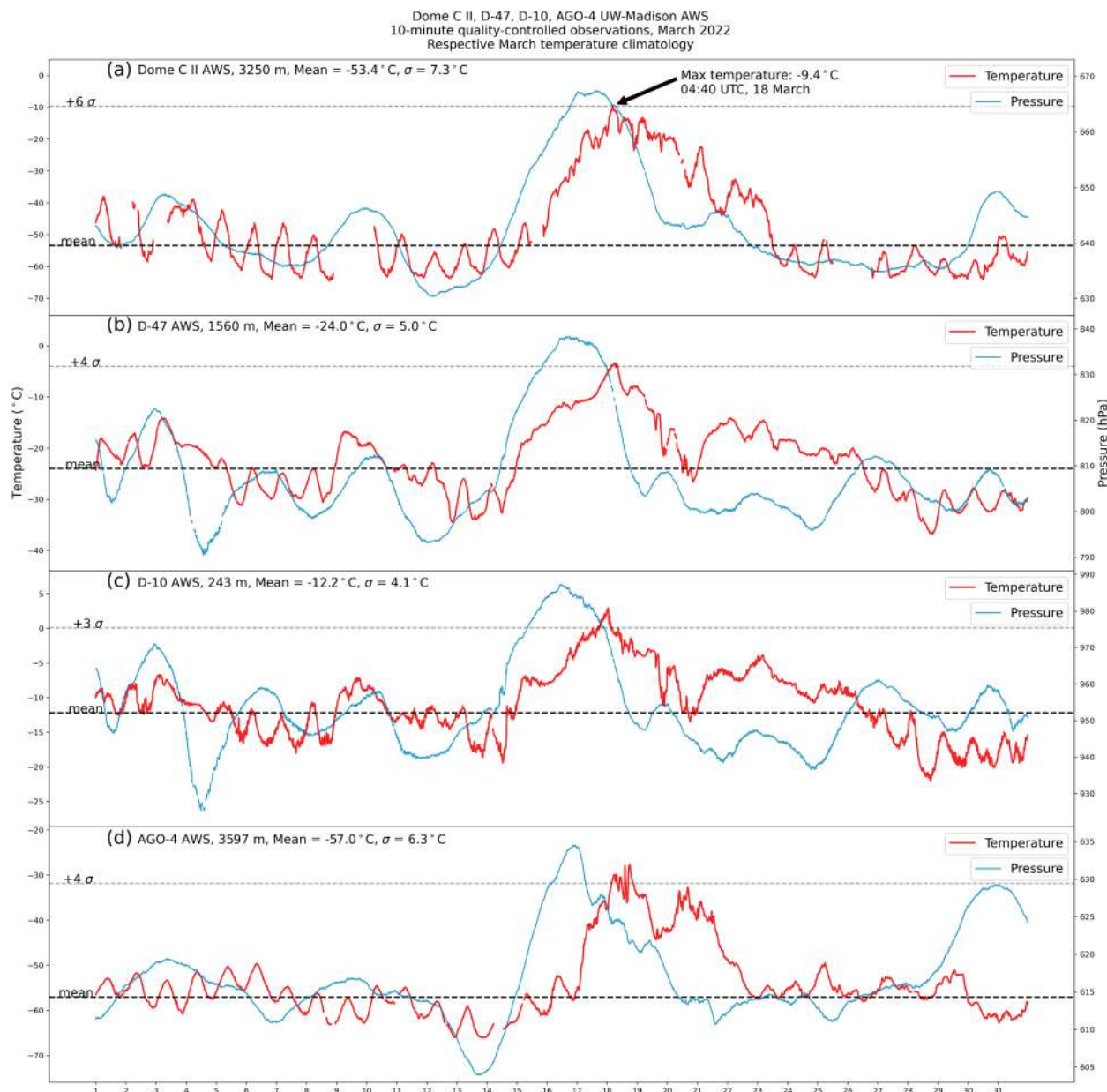


FIG. 9. March 2022 University of Wisconsin–Madison Automatic Weather Station 10-min quality-controlled temperature (red) and pressure (blue) observations and respective March temperature climatologies for (a) Dome C II, (b) D-47, (c) D-10, and (d) AGO-4. Each plot lists the AWS name, elevation, mean, and standard deviation of March 2022 temperature. The mean temperature is plotted with a thick dashed horizontal line, and the nearest integer standard deviation below the maximum temperature is plotted in a dashed horizontal line. Note the varying temperature and pressure ranges on the y axes.

the inversion layer. From 19 March onward the air above the surface inversion cooled as the AR moved away from the station and a strong surface inversion started to redevelop.

Across coastal stations in East Antarctica, the temperature increases were not as dramatic as interior observations, but still set new monthly records. Strong easterly winds were recorded by AWS at the coastal Australian Antarctic station of Casey (66.3°S, 110.5°E) from midday 16 March, during which time the surface temperature exceeded 0°C continuously for

48 h. Part of this temperature increase is likely due to foehn (downslope) winds in the lee of Law Dome. Temperature records from Wilkins ice runway (about 70 km south of Casey, altitude 753 m) exhibited a rapid rise in temperature in concert with the Casey observations, although at Wilkins the temperatures remain below 0°C. Farther to the west, and on the edge of the AR impact, vertical profiles of precipitation made with a micro rain radar MRR-PRO at Davis (68.6°S, 78°E) on 15 March indicated snowfall

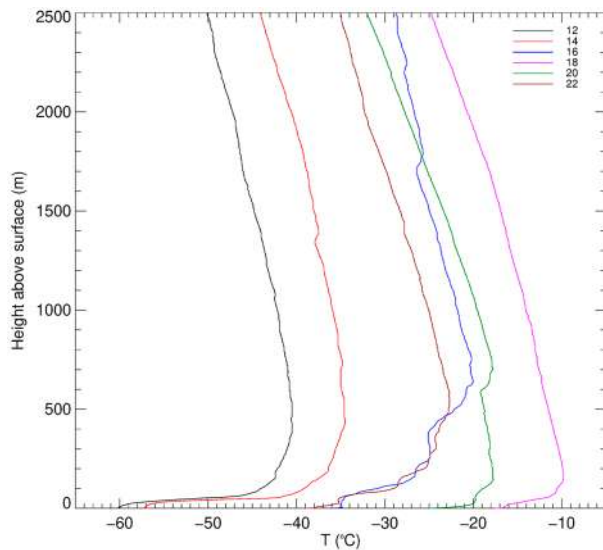


FIG. 10. Vertical temperature profiles in the lowest 2 km above Concordia Research Station (75°05′59″S, 123°19′56″E) at ~1200 UTC from 12 to 22 Mar (day of month is given in the legend).

sublimation in the lowest 1 km (not shown), due to the presence of foehn winds (Gehring et al. 2022). Temperatures from the AWS remained well below 0°C at Davis during the AR.

At Jang Bogo station, daily maximum air temperature reached 8.8°C on 18 March 2022 (and on 11 February 2022), the highest temperature recorded since official measurements began in 2014, including the summer season. The mean temperature in March over the last seven years is −14°C with intermittent high temperature (up to −2.2°C) over a short time. The highest temperature was accompanied with strong wind, starting at 0600 UTC 15 March. Maximum temperature was recorded on the issued time, and temperature returned to its normal value at 0600 UTC 21 March.

The large extent of record (or near record) temperatures at interior and coastal East Antarctic stations demonstrates the expansiveness of the heat wave. This is emphasized by ERA5 temperature data, which show an area 3.3 million km² exceeded previous March monthly temperature records (Fig. 1).

5. Implications for the Antarctic climate system

a. Event return time

Among the eight East Antarctic Ice Sheet stations, only two experienced extreme temperature or extreme anomalies during 16–18 March 2022: Dome C and Vostok. The six

remaining stations recorded highly anomalous temperatures for March, but relatively normal temperatures when compared with annual maxima (return periods much lower than 1 yr) during these three days.

On 16 March temperatures were fairly typical at Dome C and Vostok. On 17 March Dome C recorded large anomalies (return period of 8 years for minimum temperature, 3 years for maximum, and 7 years for mean). The heat-wave peak occurred on 18 March (see Table 1). It was extraordinary for the season, particularly in Vostok, giving return periods in anomalies of several hundreds of years. At Vostok, the record for anomalies was broken by 7°C for minimum temperature, by 3°C for maximum temperature, and by 6°C for mean temperature. The record in anomalies was broken at Dome C on 18 March 2022 by 3.5°C for maximum temperature and by 3°C for mean temperature (second largest anomaly in daily minimum temperature).

Given the unprecedented (since 1958) magnitude of the records broken at Vostok, the East Antarctic heat wave of 18 March 2022 was the result of an exceptional large-scale forcing situation, or an extraordinary conjunction of situations. This point is corroborated by the extreme IVT value recorded for AR, whose return time was more than 200 years at Vostok and 40 years at Dome C. Nevertheless, the more moderate return time values observed at Dome C and the absence of extreme values recorded outside of these two stations invites caution, since the extraordinary event recorded in Vostok is actually about n times more likely to happen in any of independent n stations. Using a regional approach and assuming that the eight stations are representative of East Antarctica, this transforms the 744-year return level (on TN anomaly) at Vostok into a 52-year return level at the scale of East Antarctica. Thus, other events of such magnitude are not unlikely, especially under anthropogenic climate warming.

b. Future climate implications

The historical (1980–2015) simulation ensemble from the IPSL-CM6 coupled model provides context on the extreme character of the temperature anomalies observed over the Antarctic Plateau. For each ensemble member, the daily mean temperature anomalies ΔT from the mean monthly seasonal cycle were calculated. For the future period (2035–70), the temperature anomalies were determined as departures from either the future or historical mean cycles. The frequency of occurrence of the strongest positive anomalies are plotted on Fig. 11, stratified by the monthly seasonal cycle. Different ΔT thresholds are shown, for the historical period and for the SSP3-7.0 future period with the two different reference climatologies.

TABLE 1. Return period (yr) and 95% confidence intervals (yr; in parentheses) of 18 Mar 2022 at Dome C (data back to February 1980), Vostok (data back to January 1958), and East Antarctica (see section 2 for a description).

	TN (daily min)	TX (daily max)	Tmean (daily mean)	TN anomaly	TX anomaly	Tmean anomaly
Dome C	4 (4–4)	10 (9–11)	17 (15–20)	40 (34–49)	67 (52–88)	62 (50–82)
Vostok	5 (5–5)	1 (1–2)	4 (4–4)	744 (501–1228)	172 (135–245)	855 (546–1516)
East Antarctica	2 (2–3)	<1	2 (2–2)	52 (43–67)	37 (34–42)	148 (127–177)

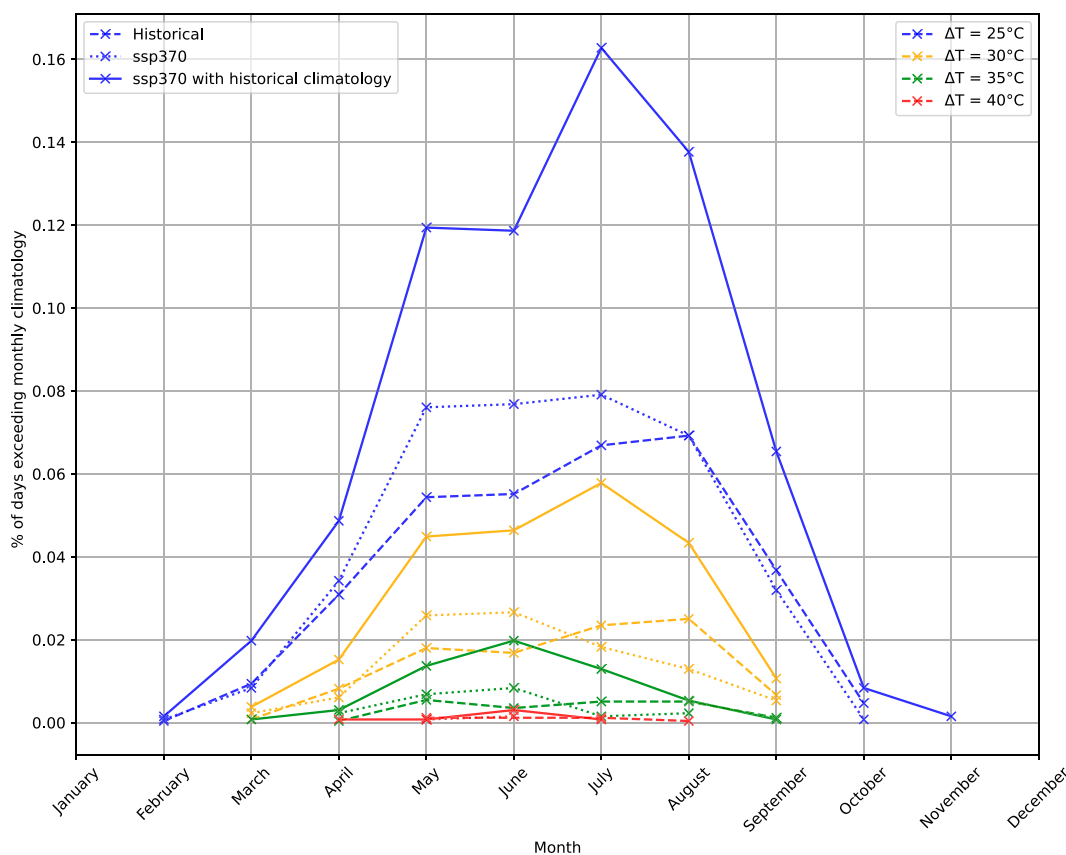


FIG. 11. Frequency of occurrence of extreme temperature anomalies simulated at Dome C from the IPSL-CM6, shown as percent of days exceeding the monthly climatology by different ΔT thresholds (colors; right-hand legend). The results are shown for the historical-period simulations (dashed lines), and for the SSP3-7.0 future period, with anomalies respective to the historical (solid lines) or future (dotted lines) periods.

Large temperature excursions are much more frequent in winter with a maximum in July but are very rare in summer given the reduced temperature variability. For the lower anomaly thresholds (different colors in Fig. 11), the frequency of occurrence more than doubles for the SSP3-7.0 future period relative to the historical one if using the same reference climatology. When using anomalies from the warmer future climatology, the distribution is closer to the present one, although it tends to be higher in late fall and early winter. Extreme events such as the one observed in March 2022 are still very rare in the model, regardless of the dataset, and do not appear to become more likely in the warmer climate according to the IPSL-CM6 simulation. Daily mean temperatures 40°C above the climatology never occur outside of the April–August period. Above 35°C happened in March only during the future period, above 30°C happened in both periods but more frequently in the future.

Because the two periods do not have the same number of years ($35 \text{ years} \times 20 \text{ members}$ for the historical period and $35 \text{ years} \times 10 \text{ members}$ for the future period), the significance of the difference in proportion between the historical period and the future period with historical climatology was tested and validated with a z -test proportion. The proportion of days

with a temperature anomaly higher than $\Delta T = 25^{\circ}\text{C}$ for the future period with historical climatology is higher than for the historical period ($p \text{ value} = 4 \times 10^{-6}$).

The return periods of this event at Dome C have been calculated for a daily mean temperature anomaly (Tmean) of $+38^{\circ}\text{C}$ (see section 2) for the historical period and the two future scenarios (SSP2-4.5 and SSP3-7.0). For each of the future scenarios, the return periods have also been calculated for an anomaly of $+38^{\circ}\text{C}$ with respect to the historical reference. Then the number of days with a $+38^{\circ}\text{C}$ anomaly in historical and future scenarios was calculated. (Table 2)

For the periods within their own reference time, the return periods of a $+38^{\circ}\text{C}$ event are similar to the results shown in section 5a using Dome C temperature data (62-yr return period). As shown in Fig. 11, the return time of the anomalies with their own reference period (historical and future) is high (54 years for SSP2-4.5, 59 years for historical, and 89 years for SSP3-7.0) when compared with the results using a historical reference average (22 years for SSP2-4.5 with historical reference and 25 years for SSP3-7.0 with historical reference), suggesting that such an event could occur with a slightly closer recurrence under future climate projections.

TABLE 2. The return time of a $+38^{\circ}\text{C}$ temperature anomaly occurring at Dome C and the number of days that same anomaly actually occurs under different IPSL-CM6 scenarios.

	Historical	SSP2-4.5	SSP3-7.0	SSP2-4.5 using historical climatology	SSP3-7.0 using historical climatology
Tmean anomaly	59 (33–108)	54 (27–101)	89 (43–193)	22 (14–32)	25 (17–39)
No. of days with an anomaly $>38^{\circ}\text{C}$	19	8	6	22	25
No. of March days with an anomaly $>38^{\circ}\text{C}$	0	0	0	1	0

However, these return periods were calculated over the whole year, so it is worth noting that a $+38^{\circ}\text{C}$ Dome C anomaly event in March is observed only once, with all periods and anomaly determination methods combined, in the SSP2-4.5 anomalies with historical reference on 28 March 2035 of the ensemble member r3i1p1f1 (Tmean = -13.91°C and Tmean anomaly = $+38.30^{\circ}\text{C}$). These results indicate that anthropogenic warming does not seem to significantly increase the likelihood of extreme temperature anomalies like those observed during March 2022, but further analysis with a larger range of models is needed to confirm this, although models struggle to capture the anthropogenic warming signal over Antarctica (Casado et al. 2023).

These results, using a dataset of 700 years for the historical period and 350 years for the future period, confirm the exceptional nature of the 22 March event, even when climate change is taken into account. Further analysis with a larger number of ensemble members or models would be needed for a better quantification.

6. Discussion and conclusions

a. Summary of main results

The extreme heat wave experienced across much of East Antarctica from 15 to 19 March 2022 broke numerous temperature records and affected the regional environment in a multitude of ways. Our analysis indicates the crucial role of low-latitude forcing in creating the atmospheric river that transported the heat and moisture southward. Moisture reservoirs from tropical cyclones and large-scale convective anomalies initiated a Rossby wave train that created blocking conditions near the Antarctic coastline. The initial AR-related moisture transport into the tropopause via a prolonged warm conveyor belt helped shift and deepen the atmospheric block over the East Antarctica interior that conveyed the humid, warm, subtropical/midlatitude air mass deep into the Antarctic continent.

Dramatic surface warming across the high East Antarctic ice sheet of 30° – 40°C was reported, breaking March monthly temperature records across an area the size of India. One of the reasons for this was the erosion of the preexisting 20°C surface temperature inversion in addition to $\sim 30^{\circ}\text{C}$ of warming due to the change in air mass. A return time of around 150 years across East Antarctica for this scale of temperature anomaly was calculated, indicating that a similar magnitude event likely had occurred in the past and is likely to occur in

the future, although it is not necessarily more prevalent when future climate projections are considered.

b. Implications of compounding

Following the review of compound extreme events proposed by Zscheischler et al. (2020), the March 2022 event appears to have a compounding nature according to the following types:

- 1) *Temporarily compounding.* We show here that the moisture transported southward by the AR originates in the southwest Indian Ocean, where strong convective activity (tropical cyclones, active phase of the MJO, and tropical–temperate interactions over southern Africa) increased precipitable water in the air column. The available moisture in the midtroposphere then transited toward the mid-latitudes, where it contributed to intensify an atmospheric ridge that channeled and deviated it southward, thereby leading to the AR development. Generally, synoptic situations like the one described above occur in Antarctica several times per year (i.e., amplification of Rossby waves, leading to strong advection of heat and moisture from relatively low latitudes to the interior of the continent in a persistent northwesterly to northeasterly flow between an extended trough and the corresponding ridge). This is usually associated with fast warming and/or increased precipitation including ARs, albeit typically not as impressively as observed here (Enomoto et al. 1998; Gorodetskaya et al. 2014; Hirasawa et al. 2000; Massom et al. 2004; Schlosser et al. 2010; Udy et al. 2021; Pohl et al. 2021; Udy et al. 2022). In this case, the phasing of multiple tropical convection anomalies leading to one large Rossby wave train greatly amplifying the jet pattern had to come together rather precisely and this event could have easily been less spectacular if small differences in timing or phasing had occurred. Plus, the record low sea ice extent present at the time of the AR may have affected the extent of moisture transport toward the continent.
- 2) *Potentially spatially compounding.* The development of the atmospheric ridge occurred within a strong zonal wave 3 pattern over the Southern Ocean. This pattern promoted strong meridional mass and moisture fluxes, part of which provided favorable conditions for AR development off the East Antarctica coastlines. The same highly perturbed circulation pattern could have favored extreme floods over New Zealand days later, which were embedded in a strong moisture transport from the subtropical to the middle latitudes. This is further supported by

a previous back-trajectory analysis that showed warm-air and moisture advection from the Great Australian Bight four days before the AR event in 18 March (Blanchard-Grigglesworth et al. 2023). Despite the co-occurrence of both hazards in these two neighboring regions, the link between both extremes remains to be assessed in detail to date.

The compounding nature of the event illustrates how extreme weather or climate conditions can lead to major impacts affecting large regions in many ways. AR activity is expected to increase around the Southern Ocean (Espinoza et al. 2018; O'Brien et al. 2022), but uncertainty remains on how this will influence moisture intrusions on the Antarctic continent.

c. Implications for calculating the return period

Assessing the rareness of extreme events (e.g., using the so-called extreme value theory) requires long, continuous and quality-controlled time series. The availability of such observations over the East Antarctic plateau at Vostok (daily measurements are performed there since 1958) and Dome C (daily observation is available since 1980) allowed a robust estimation of the return period of an event that produced anomalies like those recorded on 18 March 2022. Our estimations indicate a return period of a few decades at Dome C (between 50 and 82 years for daily mean temperature anomalies), but up to a few centuries at Vostok (546 to 1516 years). These large differences in return times highlight the sparseness of AWS observations on the East Antarctic Plateau.

Furthermore, assessing the rareness of the same event in terms of moisture transport is even more challenging. When analyzing case studies like the March 2022 event, IVT values over the Southern Ocean (one of the least instrumented and monitored regions in the world) could only be obtained through atmospheric reanalyses, and their reliability is questionable prior to the satellite era (i.e., before the late 1970s; Marshall et al. 2022). Long-term changes in moisture transport remain an issue of major importance under climate change, due to the expected increase in AR frequency and IVT associated with the Clausius-Clapeyron relationship. These long-term evolutions combine with changes in the general circulation and in the storm tracks (Chemke 2022), which modify the dynamical properties of ARs in turn (Ma et al. 2020; Payne et al. 2020). Hence, major ARs like those discussed here, are expected to occur more frequently in the future decades. Such changes, co-occurring with changes in the 0°C isotherm over the Antarctica coastlines, raise the question of the future contribution of ARs to the surface mass balance over the ice sheet. Detection and attribution studies are therefore needed not only to estimate anthropogenic influence on changes in the climate of Antarctica, but also to assess the future changes in the return period of such major ARs.

d. Research collaboration and diversity

This study represents the first part of a wide-ranging preliminary study into each aspect of the March 2022 heat wave providing context for further future exploration into each of these aspects. Each aspect explored in this study was conducted by experts related to the field and then combined to

form a cohesive narrative. The initial motivation behind this study was a universal interest in the East Antarctica heat wave shortly after its occurrence that became an open invitation discussion that led to a broad research project. As the March 2022 heat wave and related AR affected many different national Antarctic stations, an international effort was needed to gather data from all affected parties. The large, extreme impacts from this storm and heat wave created hazardous operational conditions for multiple international Antarctic operations. For example, warm temperatures close runways at Casey and McMurdo; meltwater, unstable ice, early breakouts, or slow freezing events affect travel routes and safety on land, ice or water; thicker or more extensive sea ice increases fuel and resource consumption, reducing efficiency; heavy precipitation reduces visibility, can increase cold injury occurrence, and makes outdoor activities more difficult or dangerous; and collapsing ice shelves increase the navigational hazards in regions that may have previously been ice free (COMNAP 2015; Dawson et al. 2017; Tozer et al. 2020; V. J. Heinrich and J. Lieser 2022, personal communications). Growing interest in Antarctica is leading to more people and organizations operating in these remote and extreme environments (Dawson et al. 2017).

This growth in Antarctic logistical operations coincides with an ongoing effort for more international collaboration in Antarctic science to combine the limited resources of countries conducting research in the Antarctic to create a dense network of observations. The authorship list of this study reflects this spirit, with representation from many European countries, the United States, Australia, New Zealand, South Korea, the United Arab Emirates, and Chile. It also demonstrates the need for further outreach; China is not represented despite having a large Antarctic presence. We hope that our horizontal research organizational effort and diversity serve as a good example for future Antarctic projects.

Acknowledgments. All authors particularly thank the national polar institutes such as the U.S. Antarctic Program, the French Polar Agency (IPEV), and the Australian Antarctic Division (AAD), without which none of the data used here would be available. Authors P. M. Rowe and X. Zou are grateful for funding from the National Science Foundation (NSF) Office of Polar Programs under awards 2127632 and 2229392. Author R. T. Datta is grateful for funding from NSF Office of Polar Programs award 1952199 and NASA award S000885. The PWRF model is developed and maintained by the Polar Meteorology Group, Byrd Polar and Climate Research Center (BPCRC), The Ohio State University. PWRF simulations were performed on the San Diego Supercomputing Center's COMET resource through AR Program, Phase II 460001361 and III 4600014294 (State of California, Department of Water Resources). Authors J. D. Wille and V. Favier acknowledge support from the French Agence Nationale de la Recherche projects ANR-20-CE01-0013 (ARCA). Authors C. Amory and C. Kittel appreciate the computational resources provided by the Consortium des Équipements de Calcul Intensif (CÉCI), funded by the Fonds de la Recherche Scientifique de Belgique (F.R.S.-FNRS).

Authors M. A. Lazzara and D. Mikolajczyk are grateful for support from the NSF Office of Polar Programs under grants 1924730, 1951720, and 1951603. We also thank Bella Onsi for her assistance. This project received grant funding from the Australian government as part of the Antarctic Science Collaboration Initiative program. Authors I. J. Smith and G. H. Leonard were supported by grant MFP-UOO1825 from the Marsden Fund Council from government funding, administered by the Royal Society of New Zealand, and the Antarctic Science Platform (MBIE SSIF Programmes Investment contract ANTA1801). Author C. A. Shields was supported by the U.S. Department of Energy, Office of Science, Office of Biological and Environmental Research (BER), Regional and Global Model Analysis (RGMA) component of the Earth and Environmental System Modeling Program, DE-SC0022070, NSF IA 1947282, and NCART NSF Cooperative Agreement 1852977. The National Center for Atmospheric Research is sponsored by the National Science Foundation. Author S. P. Alexander was supported by the Australian Antarctic Division's Australian Antarctic Science projects 4387 and 4637. We thank the Australian Bureau of Meteorology and the Australian Antarctic Division for providing the AWS data from the Australian Antarctic stations. Author S. González-Herrero was supported by the research group ANTALP (Antarctic, Arctic, Alpine Environments; 2017-SGR-1102) funded by the Agència de Gestió d'Ajuts Universitaris i de Recerca of the government of Catalonia. Authors S.-J. Kim and T. Choi were supported by the Korea Polar Research Institute (KOPRI) project "Understanding of Antarctic climate and environment and assessments of global influence" (PE23030) funded by the Ministry of Oceans and Fisheries. Author D. Udy was supported by an Australian Research Training scholarship and an Australian Research Council (ARC) Centre of Excellence for Climate Extremes top-up scholarship. Author T. Vance acknowledges support from the Australian Antarctic Program Partnership (ASCI000002). Udy and Vance also acknowledge support from ARC DP220100606. Author I. Ollivier was supported by the project DEEPICE. This project has received funding from the European Union's Horizon 2020 research and innovation programme under the Marie Skłodowska-Curie grant agreement 955750. Author L. D. Trusel acknowledges support from the NASA Cryospheric Sciences Program (Award 80NSSC20K0888). Author N. Wever was supported by the Swiss National Science Foundation (SNSF Grant 200020-179130). Author D. Bozkurt acknowledges support from ANID-FONDAP-1522A0001 and COPAS COASTAL ANID FB210021. Author I. V. Gorodetskaya expresses thanks for support by the strategic funding to CIIMAR (UIDB/04423/2020 and UIDP/04423/2020) and 2021.03140.CEECIND through national funds provided by the Fundação para a Ciência e a Tecnologia (FCT). Author R. D. Garreaud acknowledges support from ANID-FONDAP-1522A0001 and FONDECYT 1211412.

Data availability statement. We thank Météo France for launching daily radiosoundings at Dumont d'Urville station and for making the data freely accessible online (https://donneespubliques.meteofrance.fr/?fond=produit&id_produit=

[97&id_rubrique=33](https://doi.org/10.48567/x7a9-cx26)). Automatic Weather Station observations and Antarctic composite satellite imagery were made available from the Antarctic Meteorological Research and Data Repository (<https://doi.org/10.48567/x7a9-cx26> and <https://doi.org/10.48567/cfxm-4c37>, respectively). Australian AWS observations are freely available from the Australian Antarctic Data Centre (<https://data.aad.gov.au>). Scott Base weather station data are available from The National Climate Database (<https://cliflo.niwa.co.nz>; last accessed 11 January 2023). Radiosonde data were obtained from IPEV/PNRA Project "Routine Meteorological Observation at Station Concordia" (<http://www.climantartide.it>).

APPENDIX A

Further Analysis of the Surface Energy Balance

a. Breakdown of the surface energy balance components during the heat wave

For the 5-day mean, the large positive deviations in the SEB over the area affected by the heat wave are largely attributable to cloud-induced increases in downwelling longwave radiation ($20\text{--}45\text{ W m}^{-2}$ above average; Figs. A1d,e). In keeping with the observations at Concordia Station, SNOWPACK results indicate that the large increases in downwelling longwave radiation, due mainly to clouds, were not offset by decreases in shortwave radiation (Fig. A1a). Rather, the decreases in shortwave radiation were relatively small over the East Antarctic Ice Sheet ($15\text{--}20\text{ W m}^{-2}$ below average; Fig. A1b). The net longwave and net shortwave were 2–5 standard deviations above and below the climatological mean, respectively (Figs. A1c,f). Contributions from sensible heat flux to the total energy balance were small (Figs. A1g,h) and insignificant (Fig. A1i) because in cloudy conditions, snow surface temperature equilibrates close to the air temperature, and latent heat flux values are positive but small ($0\text{--}5\text{ W m}^{-2}$; Figs. A1j,k).

The extensive cloud cover reduced incoming solar radiation substantially, more than twice the standard deviation below the value for the climatology (Fig. A1c). However, due to the generally high albedo of the Antarctic ice sheet (AIS), the effect on the actual absorbed shortwave radiation was relatively small. The net shortwave radiation was around $5\text{--}10\text{ W m}^{-2}$ in the area affected by the heat wave (Figs. A1a,b), yet the highest positive net shortwave found on the full AIS was only about 20 W m^{-2} more. The mean net longwave radiation over the 5-day period is -10 W m^{-2} in the affected area (Fig. A1c), whereas the areas with high net shortwave radiation (and thus minimal cloud cover) exhibited 80 W m^{-2} less net longwave radiation. This demonstrates the strong impact of cloudiness from the heat-wave event on the total energy balance (Figs. A1d,e).

The turbulent fluxes, consisting of the sensible and latent heat flux, are strongly dependent on wind speed. Thus, locally highest values can be found in katabatic zones near the coastal areas (Figs. A1g,j). The sensible heat flux over the 5-day period (Fig. A1g) is positive (i.e., directed toward the surface) everywhere, since radiative cooling generally reduces surface

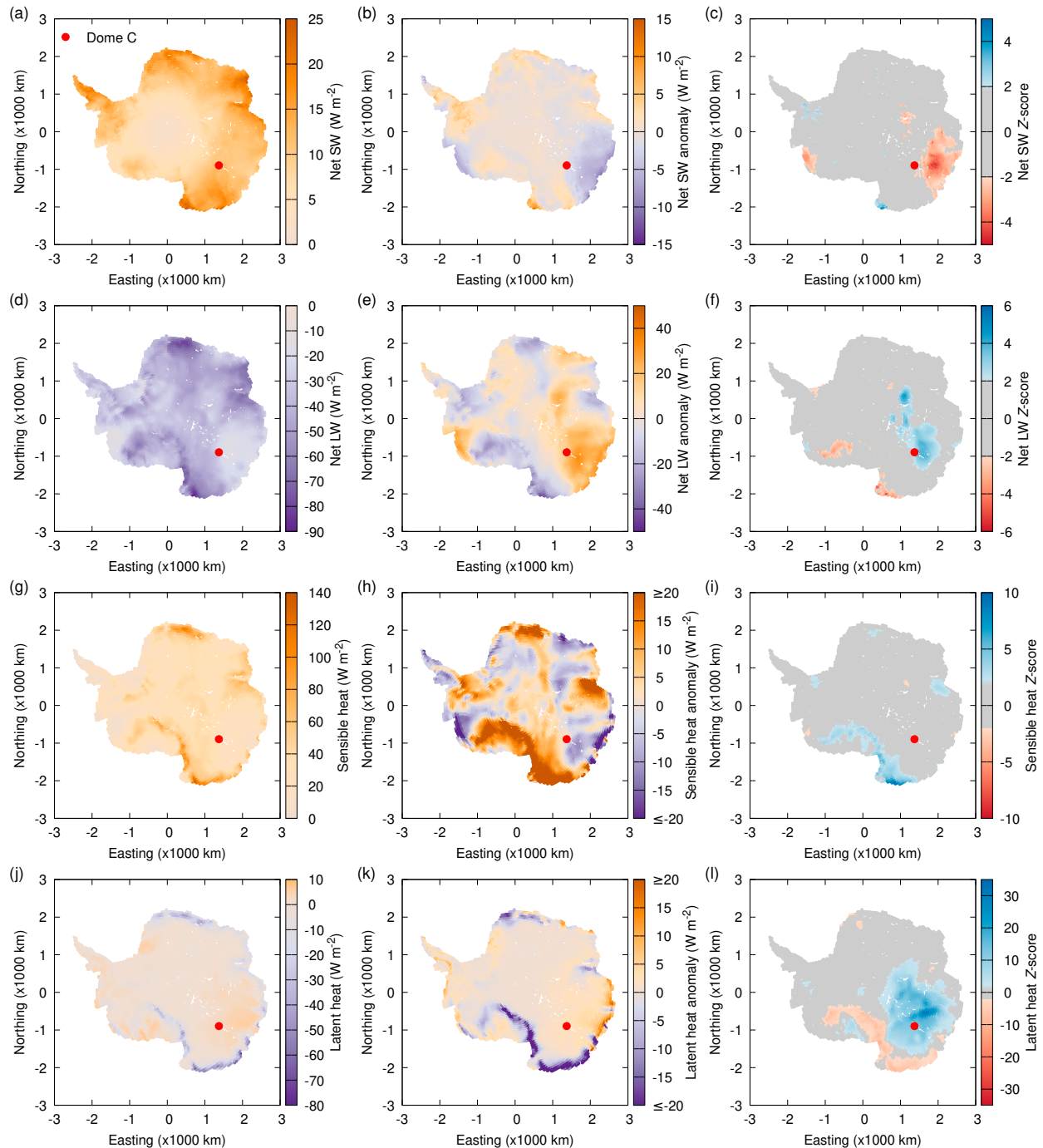


FIG. A1. Average energy balance components from SNOWPACK for (a),(b),(c) net shortwave radiation, (d),(e),(f) net longwave radiation, (g),(h),(i) sensible heat, and (j),(k),(l) latent heat. Shown are (left) the average value over the period 14–19 Mar 2022, (center) the deviation of the 2022 period from the 14 to 19 Mar 1980–2021 climatology, and (right) Z score of the 2022 anomaly. Positive values denote energy fluxes directed downward (toward the surface). Easting and northing are in the EPSG 3031 coordinate system (Antarctic polar stereographic projection). Note that in (h) and (k) the color bar has been restricted between -20 and $+20 \text{ W m}^{-2}$ to maintain detail in the area of interest.

temperatures below the air temperature. Under cloud cover, radiative cooling is compensated for by increased downwelling longwave radiation, resulting in surface temperatures equilibrating with air temperature. Therefore, in the areas affected

by the heat wave, sensible heat flux is small (less than 10 W m^{-2}) despite the warm-air advection. In some areas affected by the heat flux, the sensible heat flux was below the climatological mean (Fig. A1h), since typically the

snow surface is colder than the air, resulting in a downward sensible heat flux. With the cloudy weather, this sensible heat flux was reduced, albeit not significantly from a climatological point of view (Fig. A1i).

The heat advection was accompanied by humid air, which leads to moisture deposition on the surface and the release of latent heat (Figs. A1j,k). This is the opposite of the surface sublimation typically occurring over the AIS. Even though the absolute value is not extreme (approximately similar value, but opposite sign of the net shortwave radiation), the deviation from the climatological mean is the largest of all energy balance components (Figs. A1k,l).

APPENDIX B

Meteorological Observations in the Field

Figure 1 shows a map of Antarctica with the stations considered in this work indicated.

a. Automatic weather stations

Near-surface temperature (1.8 and 1.2 m at Australian Antarctic stations) and wind (4 m) measurements from automatic weather stations (AWS; see the summary in Table S1 in the online supplemental material) were used from five stations in East Antarctica. AWS measurements made each minute were averaged over 10 min for this analysis. Since 1980 the Antarctic Meteorological Research Center (AMRC) has installed many Automatic Weather Stations (AWS) on the Antarctic Plateau that send their data back via satellite. This project was developed and fine tuned to remedy the few meteorological observations in the interior of Antarctica (Stearns et al. 1993). The AWS collects many meteorological parameters. The temperature data are detected at one or two heights above the surface. The temperature measurements are affected by the accumulation or ablation of the snow beneath the sensor and the power system to capture and transmit the observations. In the summer months, solar radiation can affect the sensor in the event of wind speeds below 3 m s^{-1} (Genthon et al. 2011). This was not the case here, as temperature extremes were recorded when wind speeds were observed to be much faster, up to 7 m s^{-1} . The coastal Australian Antarctic stations have AWS operations extending farther back into the mid-twentieth century and provide records of the usual meteorological parameters. Davis station additionally hosts cloud and precipitation instrumentation used for research, including a micro rain radar, which was deployed as part of the Year of Polar prediction (YOPP) winter 2022 cross-Antarctic campaign and collected data during the AR event. Routine meteorological measurements have been carried out since May 2014 at Jang Bogo Station on the coastal region of Terra Nova Bay, Antarctica (74.5°S , 163°E).

b. Station temperature measurement lengths

Temperature records from Vostok station were used dating back to January 1958 (48 months are missing in the dataset: January 1962–January 1963, February–November 1994, January–December 1996, and February 2003–February 2004).

We also updated the historical temperature and wind speed database proposed by Turner et al. (2021) for Amundsen Scott (since January 1957), Casey (since February 1969), Davis (from February 1957), Dome C (since February 1980), Dumont d'Urville (since April 1956), Mawson (since February 1954), and McMurdo (since March 1956) stations. Instantaneous temperature is available at these stations every 3 h up to the end of March 2022.

c. Concordia research station

Radiosondes (Vaisala, Inc., RS92) launched daily at around 1200 UTC at Concordia were used. The radiosondes provide vertical profiles of pressure, temperature, humidity and wind speed and direction through the troposphere and lower stratosphere with a vertical resolution of about 5 m.

REFERENCES

- Agosta, C., and Coauthors, 2019: Estimation of the Antarctic surface mass balance using the regional climate model MAR (1979–2015) and identification of dominant processes. *Cryosphere*, **13**, 281–296, <https://doi.org/10.5194/tc-13-281-2019>.
- Andernach, M., J. V. Turton, and T. Mölg, 2022: Modeling cloud properties over the 79 N Glacier (Nioghalvfjærdsfjorden, NE Greenland) for an intense summer melt period in 2019. *Quart. J. Roy. Meteor. Soc.*, **148**, 3566–3590, <https://doi.org/10.1002/qj.4374>.
- Bergstrom, D. M., E. J. Woehler, A. Klekociuk, M. J. Pook, and R. Massom, 2018: Extreme events as ecosystems drivers: Ecological consequences of anomalous Southern Hemisphere weather patterns during the 2001/02 austral spring-summer. *Adv. Polar Sci.*, **29**, 190–204, <https://doi.org/10.13679/j.advps.2018.3.00190>.
- Blanchard-Whigglesworth, E., T. Cox, Z. I. Espinosa, and A. Donohoe, 2023: The largest ever recorded heatwave—Characteristics and attribution of the Antarctic heatwave of March 2022. *Geophys. Res. Lett.*, **50**, e2023GL104910, <https://doi.org/10.1029/2023GL104910>.
- Boucher, O., and Coauthors, 2020: Presentation and evaluation of the IPSL-CM6A-LR climate model. *J. Adv. Model. Earth Syst.*, **12**, e2019MS002010, <https://doi.org/10.1029/2019MS002010>.
- Bozkurt, D., R. Rondanelli, J. C. Marín, and R. Garreaud, 2018: Foehn event triggered by an atmospheric river underlies record-setting temperature along continental Antarctica. *J. Geophys. Res. Atmos.*, **123**, 3871–3892, <https://doi.org/10.1002/2017JD027796>.
- Browning, K. A., 1986: Conceptual models of precipitation systems. *Wea. Forecasting*, **1**, 23–41, [https://doi.org/10.1175/1520-0434\(1986\)001<0023:CMOPS>2.0.CO;2](https://doi.org/10.1175/1520-0434(1986)001<0023:CMOPS>2.0.CO;2).
- Carlson, T. N., 1980: Airflow through midlatitude cyclones and the comma cloud pattern. *Mon. Wea. Rev.*, **108**, 1498–1509, [https://doi.org/10.1175/1520-0493\(1980\)108<1498:ATMCAT>2.0.CO;2](https://doi.org/10.1175/1520-0493(1980)108<1498:ATMCAT>2.0.CO;2).
- Casado, M., R. Hébert, D. Faranda, and A. Landais, 2023: The quandary of detecting the signature of climate change in Antarctica. *Nat. Climate Change*, **13**, 1082–1088, <https://doi.org/10.1038/s41558-023-01791-5>.
- Chemke, R., 2022: The future poleward shift of Southern Hemisphere summer mid-latitude storm tracks stems from ocean coupling. *Nat. Commun.*, **13**, 1730, <https://doi.org/10.1038/s41467-022-29392-4>.

- , Y. Ming, and J. Yuval, 2022: The intensification of winter mid-latitude storm tracks in the Southern Hemisphere. *Nat. Climate Change*, **12**, 553–557, <https://doi.org/10.1038/s41558-022-01368-8>.
- Clem, K. R., D. Bozkurt, D. Kennett, J. C. King, and J. Turner, 2022: Central tropical Pacific convection drives extreme high temperatures and surface melt on the Larsen C Ice Shelf, Antarctic Peninsula. *Nat. Commun.*, **13**, 3906, <https://doi.org/10.1038/s41467-022-31119-4>.
- Coles, S., 2002: An introduction to statistical modeling of extreme values. *J. Amer. Stat. Assoc.*, **97**, 1204, <https://doi.org/10.1198/jasa.2002.s232>.
- Collow, A. B. M., and Coauthors, 2022: An overview of ARTMIP's tier 2 reanalysis intercomparison: Uncertainty in the detection of atmospheric rivers and their associated precipitation. *J. Geophys. Res. Atmos.*, **127**, e2021JD036155, <https://doi.org/10.1029/2021JD036155>.
- COMNAP, 2015: COMNAP Sea Ice Challenges Workshop. COMNAP Workshop Rep., 37 pp., https://www.comnap.aq/s/COMNAP_Sea_Ice_Challenges_BKLT_Web_Final_Dec2015.pdf.
- Cook, K. H., 2001: A Southern Hemisphere wave response to ENSO with implications for southern Africa precipitation. *J. Atmos. Sci.*, **58**, 2146–2162, [https://doi.org/10.1175/1520-0469\(2001\)058<2146:ASHWRT>2.0.CO;2](https://doi.org/10.1175/1520-0469(2001)058<2146:ASHWRT>2.0.CO;2).
- Corbea-Pérez, A., J. F. Calleja, C. Recondo, and S. Fernández, 2021: Evaluation of the MODIS (C6) daily albedo products for Livingston Island, Antarctic. *Remote Sens.*, **13**, 2357, <https://doi.org/10.3390/rs13122357>.
- Dawson, J., and Coauthors, 2017: Navigating weather, water, ice and climate information for safe polar mobilities. WMO Tech. Rep. WWRP/PPP 5–2017, 84 pp., <https://core.ac.uk/download/pdf/149404002.pdf>.
- Djouma, G., and D. M. Holland, 2021: Atmospheric rivers, warm air intrusions, and surface radiation balance in the Amundsen Sea embayment. *J. Geophys. Res. Atmos.*, **126**, e2020JD034119, <https://doi.org/10.1029/2020JD034119>.
- Efron, B., and R. J. Tibshirani, 1994: *An Introduction to the Bootstrap*. 1st ed. Chapman Hall/CRC, 456 pp.
- Enomoto, H., and Coauthors, 1998: Winter warming over Dome Fuji, East Antarctica and semiannual oscillation in the atmospheric circulation. *J. Geophys. Res.*, **103**, 23 103–23 111, <https://doi.org/10.1029/98JD02001>.
- Espinoza, V., D. E. Waliser, B. Guan, D. A. Lavers, and F. M. Ralph, 2018: Global analysis of climate change projection effects on atmospheric rivers. *Geophys. Res. Lett.*, **45**, 4299–4308, <https://doi.org/10.1029/2017GL076968>.
- Fauchereau, N., B. Pohl, C. J. C. Reason, M. Rouault, and Y. Richard, 2009: Recurrent daily OLR patterns in the southern Africa/southwest Indian Ocean region, implications for South African rainfall and teleconnections. *Climate Dyn.*, **32**, 575–591, <https://doi.org/10.1007/s00382-008-0426-2>.
- Fischer, E. M., S. Sippel, and R. Knutti, 2021: Increasing probability of record-shattering climate extremes. *Nat. Climate Change*, **11**, 689–695, <https://doi.org/10.1038/s41558-021-01092-9>.
- Francis, D., K. S. Mattingly, S. Lhermitte, M. Temimi, and P. Heil, 2021: Atmospheric extremes caused high oceanward sea surface slope triggering the biggest calving event in more than 50 years at the Amery Ice Shelf. *Cryosphere*, **15**, 2147–2165, <https://doi.org/10.5194/tc-15-2147-2021>.
- Gehring, J., É. Vignon, A.-C. Billault-Roux, A. Ferrone, A. Protat, S. P. Alexander, and A. Berne, 2022: Orographic flow influence on precipitation during an atmospheric river event at Davis, Antarctica. *J. Geophys. Res. Atmos.*, **127**, e2021JD035210, <https://doi.org/10.1029/2021JD035210>.
- Gelaro, R., and Coauthors, 2017: The Modern-Era Retrospective Analysis for Research and Applications, version 2 (MERRA-2). *J. Climate*, **30**, 5419–5454, <https://doi.org/10.1175/JCLI-D-16-0758.1>.
- Genthon, C., D. Six, V. Favier, M. Lazzara, and L. Keller, 2011: Atmospheric temperature measurement biases on the Antarctic plateau. *J. Atmos. Oceanic Technol.*, **28**, 1598–1605, <https://doi.org/10.1175/JTECH-D-11-00095.1>.
- González-Herrero, S., D. Barriopedro, R. M. Trigo, J. A. López-Bustins, and M. Oliva, 2022: Climate warming amplified the 2020 record-breaking heatwave in the Antarctic Peninsula. *Commun. Earth Environ.*, **3**, 122, <https://doi.org/10.1038/s43247-022-00450-5>.
- Gorodetskaya, I. V., M. Tsukernik, K. Claes, M. F. Ralph, W. D. Neff, and N. P. M. Van Lipzig, 2014: The role of atmospheric rivers in anomalous snow accumulation in East Antarctica. *Geophys. Res. Lett.*, **41**, 6199–6206, <https://doi.org/10.1002/2014GL060881>.
- , T. Silva, H. Schmithüsen, and N. Hirasawa, 2020: Atmospheric river signatures in radiosonde profiles and reanalyses at the Dronning Maud Land coast, East Antarctica. *Adv. Atmos. Sci.*, **37**, 455–476, <https://doi.org/10.1007/s00376-020-9221-8>.
- , and Coauthors, 2023: Compound drivers behind new record high temperatures and surface melt at the Antarctic Peninsula in February 2022. *Res. Square*, <https://doi.org/10.21203/rs.3.rs-2544063/v1>, preprint.
- Goyal, R., M. Jucker, A. Sen Gupta, H. H. Hendon, and M. H. England, 2021: Zonal wave 3 pattern in the Southern Hemisphere generated by tropical convection. *Nat. Geosci.*, **14**, 732–738, <https://doi.org/10.1038/s41561-021-00811-3>.
- Green, J. S. A., F. H. Ludlam, and J. F. R. McLveen, 1966: Isentropic relative-flow analysis and the parcel theory. *Quart. J. Roy. Meteor. Soc.*, **92**, 210–219, <https://doi.org/10.1002/qj.49709239204>.
- Harrold, T. W., 1973: Mechanisms influencing the distribution of precipitation within baroclinic disturbances. *Quart. J. Roy. Meteor. Soc.*, **99**, 232–251, <https://doi.org/10.1002/qj.49709942003>.
- Hart, N. C. G., C. J. C. Reason, and N. C. Fauchereau, 2010: Tropical–extratropical interactions over southern Africa: Three cases of heavy summer season rainfall. *Mon. Wea. Rev.*, **138**, 2608–2623, <https://doi.org/10.1175/2010MWR3070.1>.
- , —, and —, 2013: Cloud bands over southern Africa: Seasonality, contribution to rainfall variability and modulation by the MJO. *Climate Dyn.*, **41**, 1199–1212, <https://doi.org/10.1007/s00382-012-1589-4>.
- Hawkins, E., and R. Sutton, 2012: Time of emergence of climate signals. *Geophys. Res. Lett.*, **39**, L01702, <https://doi.org/10.1029/2011GL050087>.
- , D. Frame, L. Harrington, M. Joshi, A. King, M. Rojas, and R. Sutton, 2020: Observed emergence of the climate change signal: From the familiar to the unknown. *Geophys. Res. Lett.*, **47**, e2019GL086259, <https://doi.org/10.1029/2019GL086259>.
- Hersbach, H., and Coauthors, 2020: The ERA5 global reanalysis. *Quart. J. Roy. Meteor. Soc.*, **146**, 1999–2049, <https://doi.org/10.1002/qj.3803>.
- Hines, K. M., D. H. Bromwich, S.-H. Wang, I. Silber, J. Verlinde, and D. Lubin, 2019: Microphysics of summer clouds in central West Antarctica simulated by the Polar Weather Research and Forecasting model (WRF) and the Antarctic Mesoscale Prediction System (AMPS). *Atmos. Chem. Phys.*, **19**, 12 431–12 454, <https://doi.org/10.5194/acp-19-12431-2019>.

- Hirasawa, N., H. Nakamura, and T. Yamanouchi, 2000: Abrupt changes in meteorological conditions observed at an inland Antarctic station in association with wintertime blocking. *Geophys. Res. Lett.*, **27**, 1911–1914, <https://doi.org/10.1029/1999GL011039>.
- Ho, C.-H., J.-H. Kim, J.-H. Jeong, H.-S. Kim, and D. Chen, 2006: Variation of tropical cyclone activity in the South Indian Ocean: El Niño–Southern Oscillation and Madden–Julian Oscillation effects. *J. Geophys. Res.*, **111**, D22101, <https://doi.org/10.1029/2006JD007289>.
- Howat, I. M., C. Porter, B. E. Smith, M.-J. Noh, and P. Morin, 2019: The reference elevation model of Antarctica. *Cryosphere*, **13**, 665–674, <https://doi.org/10.5194/tc-13-665-2019>.
- Kain, J. S., 2004: The Kain–Fritsch convective parameterization: An update. *J. Appl. Meteor.*, **43**, 170–181, [https://doi.org/10.1175/1520-0450\(2004\)043<0170:TKCPAU>2.0.CO;2](https://doi.org/10.1175/1520-0450(2004)043<0170:TKCPAU>2.0.CO;2).
- Kuleshov, Y., L. Qi, R. Fawcett, and D. Jones, 2008: On tropical cyclone activity in the Southern Hemisphere: Trends and the ENSO connection. *Geophys. Res. Lett.*, **35**, L14S08, <https://doi.org/10.1029/2007GL032983>.
- Liebmann, B., and C. A. Smith, 1996: Description of a complete (interpolated) outgoing longwave radiation dataset. *Bull. Amer. Meteor. Soc.*, **77**, 1275–1277.
- Listowski, C., J. Delanoë, A. Kirchgaessner, T. Lachlan-Cope, and J. King, 2019: Antarctic clouds, supercooled liquid water and mixed phase, investigated with DARDAR: Geographical and seasonal variations. *Atmos. Chem. Phys.*, **19**, 6771–6808, <https://doi.org/10.5194/acp-19-6771-2019>.
- Ma, W., G. Chen, and B. Guan, 2020: Poleward shift of atmospheric rivers in the Southern Hemisphere in recent decades. *Geophys. Res. Lett.*, **47**, e2020GL089934, <https://doi.org/10.1029/2020GL089934>.
- MacLennan, M. L., and Coauthors, 2023: Climatology and surface impacts of atmospheric rivers on West Antarctica. *Cryosphere*, **17**, 865–881, <https://doi.org/10.5194/tc-17-865-2023>.
- Macron, C., B. Pohl, Y. Richard, and M. Bessafi, 2014: How do tropical temperate troughs form and develop over southern Africa? *J. Climate*, **27**, 1633–1647, <https://doi.org/10.1175/JCLI-D-13-00175.1>.
- Manabe, S., and R. J. Stouffer, 1980: Sensitivity of a global climate model to an increase of CO₂ concentration in the atmosphere. *J. Geophys. Res.*, **85**, 5529–5554, <https://doi.org/10.1029/JC085iC10p05529>.
- Marshall, G. J., R. L. Fogt, J. Turner, and K. R. Clem, 2022: Can current reanalyses accurately portray changes in Southern Annular Mode structure prior to 1979? *Climate Dyn.*, **59**, 3717–3740, <https://doi.org/10.1007/s00382-022-06292-3>.
- Massom, R. A., M. J. Pook, J. C. Comiso, N. Adams, J. Turner, T. Lachlan-Cope, and T. T. Gibson, 2004: Precipitation over the interior east Antarctic ice sheet related to midlatitude blocking-high activity. *J. Climate*, **17**, 1914–1928, [https://doi.org/10.1175/1520-0442\(2004\)017<1914:POTIEA>2.0.CO;2](https://doi.org/10.1175/1520-0442(2004)017<1914:POTIEA>2.0.CO;2).
- Nakanishi, M., and H. Niino, 2006: An improved Mellor–Yamada level-3 Model: Its numerical stability and application to a regional prediction of advection fog. *Bound.-Layer Meteor.*, **119**, 397–407, <https://doi.org/10.1007/s10546-005-9030-8>.
- Nash, D., D. Waliser, B. Guan, H. Ye, and F. M. Ralph, 2018: The role of atmospheric rivers in extratropical and polar hydroclimate. *J. Geophys. Res. Atmos.*, **123**, 6804–6821, <https://doi.org/10.1029/2017JD028130>.
- Niu, G.-Y., and Coauthors, 2011: The community Noah land surface model with multiparameterization options (Noah-MP): 1. Model description and evaluation with local-scale measurements. *J. Geophys. Res.*, **116**, D12109, <https://doi.org/10.1029/2010JD015139>.
- O'Brien, T. A., and Coauthors, 2022: Increases in future AR count and size: Overview of the ARTMIP tier 2 CMIP5/6 experiment. *J. Geophys. Res. Atmos.*, **127**, e2021JD036013, <https://doi.org/10.1029/2021JD036013>.
- Payne, A. E., and Coauthors, 2020: Responses and impacts of atmospheric rivers to climate change. *Nat. Rev. Earth Environ.*, **1**, 143–157, <https://doi.org/10.1038/s43017-020-0030-5>.
- Philip, S. Y., and Coauthors, 2022: Rapid attribution analysis of the extraordinary heat wave on the Pacific Coast of the US and Canada in June 2021. *Earth Syst. Dyn.*, **13**, 1689–1713, <https://doi.org/10.5194/esd-13-1689-2022>.
- Pohl, B., Y. Richard, and N. Fauchereau, 2007: Influence of the Madden–Julian Oscillation on southern African summer rainfall. *J. Climate*, **20**, 4227–4242, <https://doi.org/10.1175/JCLI4231.1>.
- , B. Dieppois, J. Crétat, D. Lawler, and M. Rouault, 2018: From synoptic to interdecadal variability in southern African rainfall: Toward a unified view across time scales. *J. Climate*, **31**, 5845–5872, <https://doi.org/10.1175/JCLI-D-17-0405.1>.
- , and Coauthors, 2021: Relationship between weather regimes and atmospheric rivers in East Antarctica. *J. Geophys. Res. Atmos.*, **126**, e2021JD035294, <https://doi.org/10.1029/2021JD035294>.
- Ralph, F. M., M. D. Dettinger, M. M. Cairns, T. J. Galarneau, and J. Eylander, 2018: Defining “atmospheric river”: How the *Glossary of Meteorology* helped resolve a debate. *Bull. Amer. Meteor. Soc.*, **99**, 837–839, <https://doi.org/10.1175/BAMS-D-17-0157.1>.
- , J. J. Rutz, J. M. Cordeira, M. Dettinger, M. Anderson, D. Reynolds, L. J. Schick, and C. Smallcomb, 2019: A scale to characterize the strength and impacts of atmospheric rivers. *Bull. Amer. Meteor. Soc.*, **100**, 269–289, <https://doi.org/10.1175/BAMS-D-18-0023.1>.
- , M. D. Dettinger, J. J. Rutz, and D. E. Waliser, Eds., 2020: *Atmospheric Rivers*. Springer, 252 pp.
- Risser, M. D., and M. F. Wehner, 2017: Attributable human-induced changes in the likelihood and magnitude of the observed extreme precipitation during Hurricane Harvey. *Geophys. Res. Lett.*, **44**, 12 457–12 464, <https://doi.org/10.1002/2017GL075888>.
- Schlosser, E., K. W. Manning, J. G. Powers, M. G. Duda, G. Birnbaum, and K. Fujita, 2010: Characteristics of high-precipitation events in Dronning Maud Land, Antarctica. *J. Geophys. Res.*, **115**, D14107, <https://doi.org/10.1029/2009JD013410>.
- , B. Stenni, M. Valt, A. Cagnati, J. G. Powers, K. W. Manning, M. Raphael, and M. G. Duda, 2016: Precipitation and synoptic regime in two extreme years 2009 and 2010 at Dome C, Antarctica—Implications for ice core interpretation. *Atmos. Chem. Phys.*, **16**, 4757–4770, <https://doi.org/10.5194/acp-16-4757-2016>.
- Shields, C. A., J. D. Wille, A. B. Marquardt Collow, M. MacLennan, and I. V. Gorodetskaya, 2022: Evaluating uncertainty and modes of variability for Antarctic atmospheric rivers. *Geophys. Res. Lett.*, **49**, e2022GL099577, <https://doi.org/10.1029/2022GL099577>.
- Stearns, C. R., L. M. Keller, G. A. Weidner, and M. Sievers, 1993: Monthly mean climatic data for Antarctic automatic weather stations. *Antarctic Meteorology and Climatology: Studies Based on Automatic Weather Stations*, D. H. Bromwich and C. R. Stearns, Eds., Antarctic Research Series, American Geophysical Union, 1–21.

- Takaya, K., and H. Nakamura, 2001: A formulation of a phase-independent wave-activity flux for stationary and migratory quasigeostrophic eddies on a zonally varying basic flow. *J. Atmos. Sci.*, **58**, 608–627, [https://doi.org/10.1175/1520-0469\(2001\)058<0608:AFOAPI>2.0.CO;2](https://doi.org/10.1175/1520-0469(2001)058<0608:AFOAPI>2.0.CO;2).
- Terpstra, A., I. V. Gorodetskaya, and H. Sodemann, 2021: Linking sub-tropical evaporation and extreme precipitation over East Antarctica: An atmospheric river case study. *J. Geophys. Res. Atmos.*, **126**, e2020JD033617, <https://doi.org/10.1029/2020JD033617>.
- Thompson, V., and Coauthors, 2022: The 2021 western North America heat wave among the most extreme events ever recorded globally. *Sci. Adv.*, **8**, eabm6860, <https://doi.org/10.1126/sciadv.abm6860>.
- Tozer, C., J. Risbey, S. Bluhm, and T. Remenyi, 2020: Industry engagement to identify climate sensitive decisions on multi-year timescales: TasLab engage final report. Earth Systems and Climate Change Hub Tech. Rep. 13, 36 pp., https://research.csiro.au/dfp/wp-content/uploads/sites/148/2020/04/ESCCHub_TasLabEngage_report_Final.pdf.
- Turner, J., H. Lu, J. King, G. J. Marshall, T. Phillips, D. Bannister, and S. Colwell, 2021: Extreme temperatures in the Antarctic. *J. Climate*, **34**, 2653–2668, <https://doi.org/10.1175/JCLI-D-20-0538.1>.
- , —, —, S. Carpentier, M. Lazzara, T. Phillips, and J. Wille, 2022: An extreme high temperature event in coastal East Antarctica associated with an atmospheric river and record summer downslope winds. *Geophys. Res. Lett.*, **49**, e2021GL097108, <https://doi.org/10.1029/2021GL097108>.
- Udy, D. G., T. R. Vance, A. S. Kiem, N. J. Holbrook, and M. A. J. Curran, 2021: Links between large-scale modes of climate variability and synoptic weather patterns in the southern Indian Ocean. *J. Climate*, **34**, 883–899, <https://doi.org/10.1175/JCLI-D-20-0297.1>.
- , —, —, and —, 2022: A synoptic bridge linking sea salt aerosol concentrations in East Antarctic snowfall to Australian rainfall. *Commun. Earth Environ.*, **3**, 175, <https://doi.org/10.1038/s43247-022-00502-w>.
- Wernli, H., 1997: A Lagrangian-based analysis of extratropical cyclones. II: A detailed case-study. *Quart. J. Roy. Meteor. Soc.*, **123**, 1677–1706, <https://doi.org/10.1002/qj.49712354211>.
- , and H. C. Davies, 1997: A Lagrangian-based analysis of extratropical cyclones. I: The method and some applications. *Quart. J. Roy. Meteor. Soc.*, **123**, 467–489, <https://doi.org/10.1002/qj.49712353811>.
- Wille, J. D., V. Favier, A. Dufour, I. V. Gorodetskaya, J. Turner, C. Agosta, and F. Codron, 2019: West Antarctic surface melt triggered by atmospheric rivers. *Nat. Geosci.*, **12**, 911–916, <https://doi.org/10.1038/s41561-019-0460-1>.
- , and Coauthors, 2021: Antarctic atmospheric river climatology and precipitation impacts. *J. Geophys. Res. Atmos.*, **126**, e2020JD033788, <https://doi.org/10.1029/2020JD033788>.
- , and Coauthors, 2022: Intense atmospheric rivers can weaken ice shelf stability at the Antarctic Peninsula. *Commun. Earth Environ.*, **3**, 90, <https://doi.org/10.1038/s43247-022-00422-9>.
- , and Coauthors, 2024: The extraordinary March 2022 East Antarctica “heat” wave. Part II: Impacts on the Antarctic ice sheet. *J. Climate*, **37**, 779–799, <https://doi.org/10.1175/JCLI-D-23-0176.1>.
- Xu, M., L. Yu, K. Liang, T. Vihma, D. Bozkurt, X. Hu, and Q. Yang, 2021: Dominant role of vertical air flows in the unprecedented warming on the Antarctic Peninsula in February 2020. *Commun. Earth Environ.*, **2**, 133, <https://doi.org/10.1038/s43247-021-00203-w>.
- Zhang, C., 2005: Madden-Julian Oscillation. *Rev. Geophys.*, **43**, RG2003, <https://doi.org/10.1029/2004RG000158>.
- Zou, X., D. H. Bromwich, A. Montenegro, S.-H. Wang, and L. Bai, 2021: Major surface melting over the Ross Ice Shelf. Part II: Surface energy balance. *Quart. J. Roy. Meteor. Soc.*, **147**, 2895–2916, <https://doi.org/10.1002/qj.4105>.
- , and Coauthors, 2023: Strong warming over the Antarctic Peninsula during combined atmospheric river and foehn events: Contribution of shortwave radiation and turbulence. *J. Geophys. Res. Atmos.*, **128**, e2022JD038138, <https://doi.org/10.1029/2022JD038138>.
- Zscheischler, J., and Coauthors, 2020: A typology of compound weather and climate events. *Nat. Rev. Earth Environ.*, **1**, 333–347, <https://doi.org/10.1038/s43017-020-0060-z>.